Nanoscale Horizons

REVIEW

View Article Online
View Journal | View Issue

Cite this: *Nanoscale Horiz.*, 2024, **9**, 1390

Advancements in molecular disassembly of optical probes: a paradigm shift in sensing, bioimaging, and therapeutics

Karolina Saczuk, [a] Marta Dudek, [a] Katarzyna Matczyszyn [ab] and Marco Deiana *[a]

The majority of self-assembled fluorescent dyes suffer from aggregation-caused quenching (ACQ), which detrimentally affects their diagnostic and therapeutic effectiveness. While aggregation-induced emission (AIE) active dyes offer a promising solution to overcome this limitation, they may face significant challenges as the intracellular environment often prevents aggregation, leading to disassembly and posing challenges for AIE fluorogens. Recent progress in signal amplification through the disassembly of ACQ dyes has opened new avenues for creating ultrasensitive optical sensors and enhancing phototherapeutic outcomes. These advances are well-aligned with cutting-edge technologies such as single-molecule microscopy and targeted molecular therapies. This work explores the concept of disaggregation-induced emission (DIE), showcasing the revolutionary capabilities of DIE-based dyes from their design to their application in sensing, bioimaging, disease monitoring, and treatment in both cellular and animal models. Our objective is to provide an in-depth comparison of aggregation *versus* disaggregation mechanisms, aiming to stimulate further advancements in the design and utilization of ACQ fluorescent dyes through DIE technology. This initiative is poised to catalyze scientific progress across a broad spectrum of disciplines.

Received 30th April 2024,
Accepted 18th June 2024

DOI: 10.1039/d4nh00186a

rsc.li/nanoscale-horizons

[a] *Institute of Advanced Materials, Faculty of Chemistry, Wrocław University of Science and Technology, 50-370 Wrocław, Poland. E-mail: m.deiana@pwr.edu.pl*
[b] *International Institute for Sustainability with Knotted Chiral Meta Matter (WPI-SKCM(2)), Hiroshima University, Higashi-Hiroshima, Hiroshima 739-8526, Japan*

Karolina Saczuk

Karolina Saczuk is a PhD student at the Institute of Advanced Materials, Wrocław University of Science and Technology (WUST), Poland. She earned her master's degree in Chemistry and Materials Science, along with two bachelor's degrees in Chemical Technology and Chemical and Process Engineering, both from WUST. Prior to her PhD candidacy, under the guidance of Dr Marco Deiana and Professor Katarzyna Matczyszyn, Karolina accumulated experience in the manufacturing sector, primarily within the food and automotive industries. Currently, she is focusing her research on photodynamic therapy, G-quadruplex biology, and hypoxia.

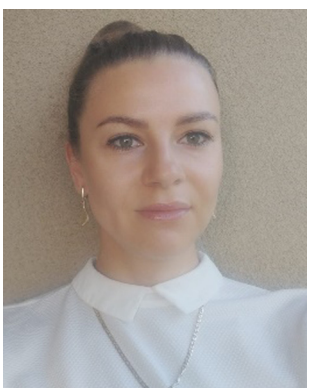

Marta Dudek

Marta Dudek is an Assistant Professor at the Institute of Advanced Materials, Wrocław University of Science and Technology (WUST), Poland. She obtained her PhD degree in 2019 in the field of Chemical Science under the guidance of Prof. Katarzyna Matczyszyn. She gained additional experience during several internships at the University of Strasbourg (France), École Normale Supérieure in Cachan (France), Institute de Sciences Chimiques de Rennes (France), Humboldt University (Germany) and Umeå University (Sweden). Her scientific interests involve the design, synthesis, and characterization of new azobenzene photoswitches as well as their application in biological settings.

1 Introduction

The self-assembly of synthetic molecular building blocks represents a powerful approach for fabricating materials with precise properties and functions.[1–3] Guided by thermodynamic principles, supramolecular systems generally attain their lowest free-energy state *via* self-assembly, with monomeric units initially in a higher free-energy state.[4] However, alternative systems involving kinetically controlled supramolecular polymerization[5–7] or out-of-equilibrium processes[8–11] may also be engineered. The dynamic balance between the assembled and unassembled states hinges on their free-energy difference, wherein the formation rate of structured assemblies generally surpasses the rate of disassembly. Such molecular aggregates arise *via* non-covalent interactions, including π–π stacking, hydrogen bonding, and dipole–dipole forces.[12,13] Specific molecular arrangements can guide self-assembly into uniform structures, such as J-type aggregates, while hydrophobic interactions in π-extended systems tend to produce heterogeneous nanoparticles of varying sizes, known as H-type aggregates.[12,14–18] These variations significantly influence the optical properties of luminescent materials and, in the context of biomedical research, their translation into clinical applications.[19,20]

Traditional fluorescent molecules are highly effective emitters when isolated, but often experience aggregation-caused quenching (ACQ) at the concentrations commonly used for sensing and imaging.[21] This phenomenon, which arises from intermolecular π-stacking, reduces their effectiveness in biological applications, although a handful of ACQ dyes have been reported to be suitable for such uses, particularly in the contexts of drug delivery[22–25] and photothermal therapy (PTT).[26] Conversely, the phenomenon of aggregation-induced emission (AIE) signifies a paradigm shift, where organic molecules emit light upon aggregation, offering a counterpoint to ACQ by promoting luminescence through the restriction of intramolecular motions.[21,27]

Despite advancements in understanding and applying AIE, integrating it into biological systems remains challenging.[28,29] This difficulty arises, for instance, because cell media typically contain serum supplements, and intracellular environments tend to reduce aggregation, leading to the disassembly of the probes.[30] These limitations underscore the necessity for innovative sensing mechanisms that can navigate the constraints of both ACQ and AIE.

Enter disaggregation-induced emission (DIE), a mechanism that harnesses signal amplification through the disassembly of aggregated probes, offering a promising alternative for probe development.[31–35] DIE involves chemical compounds that exhibit enhanced emissive properties upon interaction with specific biomolecules or analytes, effectively transforming from a self-quenched state to a highly luminescent form. Despite its potential, DIE remains a relatively underexplored area with much to offer in sensing, bioimaging, and therapeutic applications.

This review aims to summarize the advancements in the field of DIE research, with a specific focus on the development of DIE-active probes that target key macromolecules—namely nucleic acids, proteins, and lipids. These biological targets are specifically chosen as they constitute the primary focus of existing DIE research, supported by well-established and robust data.

While other elements such as macrocyclic cavitands,[36–41] signalling molecules (*e.g.*, adenosine-5′-triphosphate,[42–45] sulfur dioxide[46] or gluthatione[47]), metal ions,[48–51] and various stimuli (*e.g.*, surfactants,[52,53] pH[54–57] or temperature[58]) also play significant roles, either directly or indirectly, as disaggregating triggers, they are excluded from this review to maintain a concentrated exposition on the fundamental principles of DIE and their translational potential in advanced clinical research.

This comprehensive overview of DIE mechanisms and current research directions emphasizes the need for precise data interpretation to prevent misconceptions, especially for those

Katarzyna Matczyszyn

Katarzyna Matczyszyn is a physical chemist and a Professor at the Wrocław University of Science and Technology (WUST), Poland. She is also an affiliated member of the WPI SKMC2 at Hiroshima University, Japan. Previously, she worked at CEA Saclay, École Normale Supérieure de Cachan, and Université Pierre and Marie Curie in France. Her major scientific interest lies in light-matter interactions, particularly with biologically significant materials. She works with photoactive molecules (mostly photochromes), various types of nanoparticles (including plasmonic and carbon nanodots), lyotropic liquid crystals, and in the field of nonlinear optics. She is particularly interested in novel approaches to photodynamic therapy.

Marco Deiana

Marco Deiana is an Assistant Professor at the Institute of Advanced Materials, Wrocław University of Science and Technology (WUST), Poland. He completed his PhD in Materials Engineering at WUST in 2018 under the supervision of Prof. Katarzyna Matczyszyn. Subsequently, he joined Umeå University in Sweden as a postdoctoral fellow from 2018 to 2023, working in the research group of Prof. Nasim Sabouri. In 2023, Dr Deiana returned to WUST with a grant from the National Science Centre (NCN) to serve as the Principal Investigator. His research interests include G-quadruplex biology, hypoxia, light-activated therapies, molecular chirality, and self-assembly.

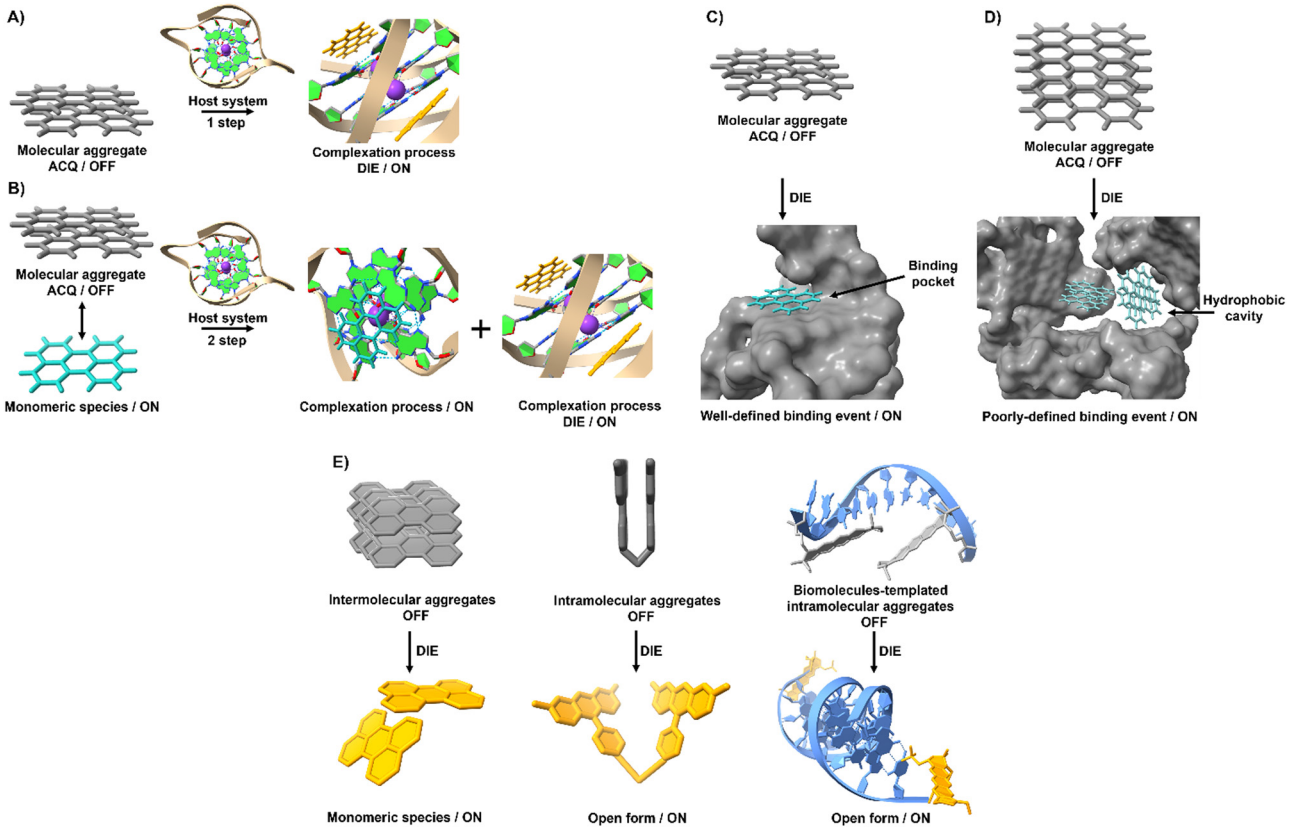

Fig. 1 Graphical illustration depicting the simplified mechanisms of molecular recognition mediated by self-assembled probes used in the design of DIE-active dyes. (A) In an aqueous environment, only molecular aggregates are formed by an ACQ-active probe. When a targeted receptor (host) is present, the aggregate state disassembles to form a complex if the free energy of the complex is lower than or similar to that governing the assembly process. (B) An equilibrium is maintained between aggregated and monomeric species. The introduction of a target receptor initiates two binding processes: initially, the monomers in solution bind to the receptor until saturation; subsequently, excess host triggers the disassembly of the aggregates. (C) Molecular recognition mediated by an intramolecularly formed biological structure with a well-defined binding pocket triggers disassembly of the optical probe, resulting in a precise binding event characterized by a specific stoichiometry. (D) Intermolecularly interacting biological matrices can form hydrophobic cavities that coordinate with self-assembled probes, driving their molecular disassembly and resulting in poorly defined complexes that do not adhere to conventional stoichiometry. (E) Various molecular arrangements of ACQ probes demonstrate DIE mechanisms through intermolecular, intramolecular, and biologically templated self-assembly aggregates.

new to the field. The discussion will highlight the challenges, limitations, and future prospects of DIE research, emphasizing its transformative potential in advancing the design and optimization of molecular probes across various applications.

2 Disaggregation-induced emission

Compounds exhibiting ACQ characteristics predominate posing significant limitations for sensor and drug development.

However, ACQ, despite its common perception as an unfavourable occurrence, can be ingeniously utilized in the design of activatable probes. This approach leverages the fact that introducing a significant alteration in the environment of ACQ-based probes can shift the equilibrium from aggregated states to their monomeric forms. This transition, occurring under specific conditions, can enhance and recover the readout signal, thereby shifting from an "OFF" to an "ON" state.

The process of leveraging ACQ for probe development can occur in at least two simplified scenarios.[59] In the simplest scenario, all molecules form molecular aggregates with ACQ character, and the transition from aggregate to monomer enhances the readout signal (Fig. 1(A)). Alternatively, an equilibrium might exist between molecular aggregates with ACQ character and monomeric species (Fig. 1(B)). In this equilibrium, complexation occurs in two steps: initially, the formation of a complex between the monomer and the host molecule at low host concentrations; and following saturation of this binding event, a second binding event at higher host concentrations leads to the disassembly of the molecular aggregates. In both scenarios, the parameters governing the disassembly process require that the association constant of the aggregated molecules ($K_{\text{aggregation}}$) be lower than or similar to the association constant resulting from the complexation with the host matrix (K_{complex}). In other words, the Gibbs free energy (ΔG) governing the aggregation process should be higher than or similar to the ΔG value resulting from the complexation event ($\Delta G_{\text{aggregation}} > \Delta G_{\text{complex}}$).

Complexation between aggregated dyes and targeted biomolecules often leads to the formation of well-defined

complexes with specific stoichiometry.[32,33,60–62] Nonlinear fitting models describing common binding stoichiometries (1 : 1, 1 : 2, or 2 : 1) usually represent experimental data accurately. These quantitative binding parameters are often associated with models such as Job's plots or mole ratio methods, which describe the system's stoichiometry. Structural investigations performed by nuclear magnetic resonance (NMR) spectroscopy or molecular dynamics (MD) simulations provide valuable insights into the molecular nature of these systems.

However, this scenario typically occurs when inter or intramolecular dye aggregates coordinate with intramolecularly formed biomolecules possessing specific binding pockets (Fig. 1(C)). The situation can become more complicated when intermolecular processes at the biological level influence the complexation process. For instance, intermolecularly interacting biological structures may create hydrophobic domains that do not selectively coordinate with molecular aggregates (Fig. 1(D)). As a result, the disassembly of the probe might not follow the expected aggregation-to-monomer transition, leading to unusual binding events, with association curves that do not exhibit saturation even in the presence of high concentrations of biological templates.

Understanding these complex interactions requires further investigation, as the interplay between dye aggregates and biological structures can significantly impact the efficiency and accuracy of DIE dyes in practical applications.

To harness ACQ effectively for DIE, two main rational design strategies have been proposed, focusing on either intermolecular[32,35,61,62] or intramolecular[34,63,64] self-assembly (Fig. 1(E)). Intermolecular aggregation typically leads to the formation of supramolecular structures with loosely defined arrangements. In contrast, intramolecular aggregation results in well-defined systems, facilitating precise and controlled self-assembly. Further, incorporating biological templates[65,66] into the supramolecular assembly process can optimize ACQ dyes for optical performance in DIE-based sensing applications.

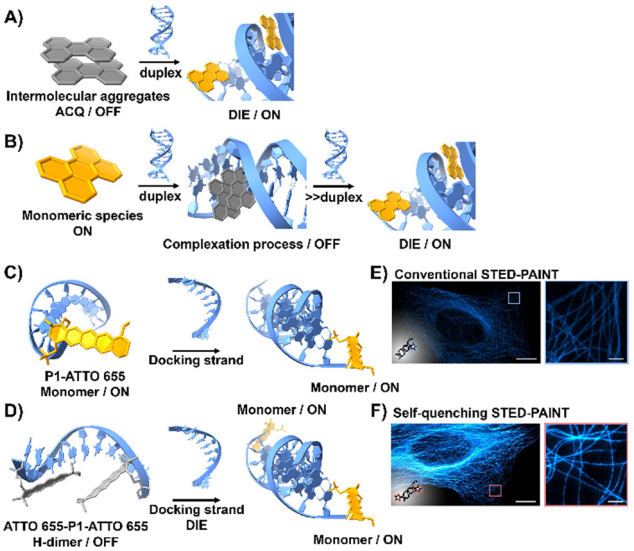

Fig. 2 (A) Intermolecular aggregates exhibiting ACQ characteristics can transform into highly emissive monomeric species bound to duplex DNA through the DIE mechanism. (B) In the presence of low concentrations of duplex DNA, the highly emissive monomeric state of a probe self-assembles within the grooves, rather than at intercalation sites. At higher duplex concentrations, a new competitive equilibrium forms between pre-existing DNA-dye aggregates and monomer-like DNA complexes through the DIE process. (C) and (D) Schematic diagrams of optical designs include: (C) the single ATTO 655 dye attached to the 3′-end of the imager strand (**P1-ATTO 655**), and (D) two ATTO 655 dyes at both the 5′- and 3′-ends of the imager strand, forming a self-quenching H-type dimer (**ATTO 655-P1-ATTO 655**). Upon introduction of the complementary docking strand, the H-dimer disassembles, leading to a significant increase in fluorescence. (E) and (F) STED microscopy images of U2OS cells immunolabeled for microtubules using either **P1-ATTO 655** (E) or the dual-labelled **ATTO 655-P1-ATTO 655** (F), demonstrating the effects of dye placement and configuration on fluorescence enhancement. The scale bars represent 10 μm for overviews and 1 μm for detailed zoom-ins. Reproduced from ref. 66 with permission from the Wiley-VCH.

3 Biomolecules-mediated DIE

DIE-active dyes, either used independently or in conjunction with various biomolecules, have led to the creation of ultra-sensitive fluorogenic agents boasting exceptional recognition and imaging properties. The subsequent sections delve into the assembly and utilization of this category of materials, focusing on their interaction with different biomolecules: nucleic acids, proteins, and lipids.

3.1 DNA-mediated DIE

DNA is essential to the central dogma of molecular biology, functioning not only as a repository for genetic information but also playing a key role in various biological processes with significant clinical implications.[67,68] So far, only a limited number of probes that interact directly with double-stranded (ds) DNA have demonstrated DIE character.[69,70] They function by directly disassembling upon binding to dsDNA, either through a single-step disassembly mechanism[69] or by undergoing a DNA-templated aggregation process first, followed by disassembly at higher duplex concentrations[70] (Fig. 2(A) and (B)).

Heilemann and colleagues have proposed an intriguing application of DNA-labelled DIE-active dyes to enhance super-resolution imaging techniques.[66] They developed a short-distance H-type self-quenched fluorophore dimer, utilizing the oxazine fluorophore ATTO 655 attached to both the 5′- and 3′-ends of a 9 nucleotide-long DNA imager strand (P1) (**ATTO 655-P1-ATTO 655**), and assessed its performance against a version labelled with a single ATTO 655 dye at the 3′-end (**P1-ATTO 655**) (Fig. 2(C) and (D)).[66] Spectroscopic analysis revealed that the dual-labelled strand **ATTO 655-P1-ATTO 655** shifted from a weakly emissive H-type dimer to a highly fluorescent monomeric state upon forming the docking-imager duplex, markedly enhancing fluorescence and stability. The use of the dual-labelled strand in stimulated emission depletion (STED) imaging[71] of immunolabeled α-tubulin in human osteosarcoma U2OS cells resulted in a significant improvement in image quality, achieving a five-fold increase in signal-to-background ratio (SBR) compared to the single-labelled strand (Fig. 2(E) and (F)).[66]

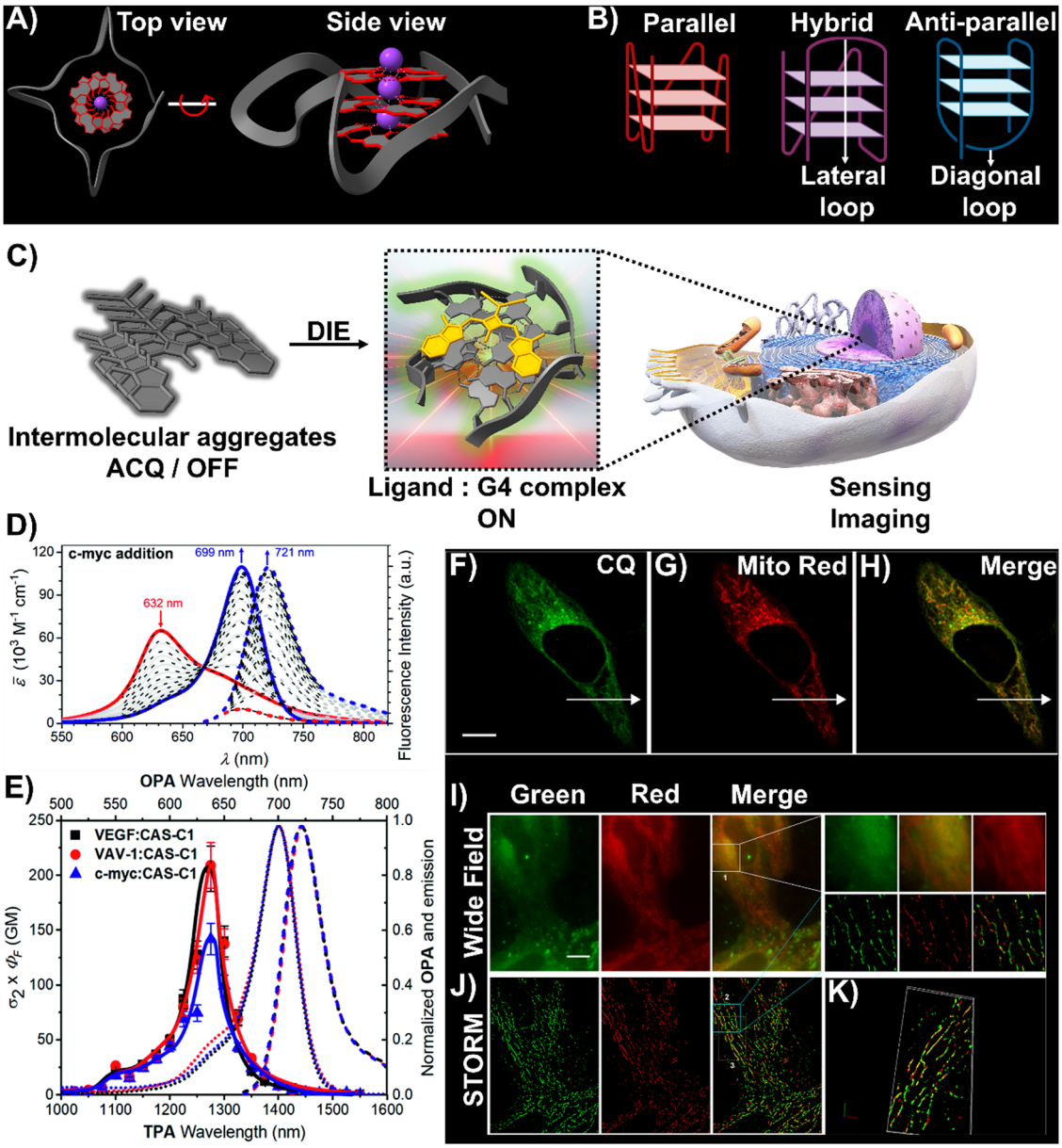

Fig. 3 (A) Visualization of G4 structures with top and side views of the X-ray crystallographic structure of parallel human telomeric DNA G-quadruplex (PDB: 1KF1). (B) Depiction of G4 structures forming various topologies: parallel, hybrid, and antiparallel. White arrows indicate lateral and diagonal loops in hybrid and antiparallel G4s, respectively. Created with BioRender.com. (C) Schematic of the DIE process facilitated by G4 structures. (D) Spectrophotometric and fluorometric analyses of the **CAS-C1** molecule with incremental additions of the *c-MYC* G4. (E) Graph showing the two-photon molecular brightness ($\sigma_2 \times \Phi_F$) of the **CAS-C1** complex with G4 structures from *VEGF*, *VAV-1*, and *c-MYC*. Reproduced from ref. 33 with permission from the Royal Society of Chemistry. (F)–(H) Colocalization studies using **CQ** compound (F), MitoTracker Red CMXRos (G), and their merged imaging (H) in live HepG2 cells. (I) and (J) Widefield (I) and reconstructed STORM images (J) of HepG2 cells stained with **CQ** and MitoTracker Red CMXRos, including magnified views. Scale bar: 10 μm. (K) Three-dimensional volume representation of STORM-based colocalization between **CQ** and MitoTracker Red CMXRos. Reprinted with permission from ref. 81. Copyright 2021 American Chemical Society.

By applying the principles of hybridization and fluorogenic dimers, the sensitivity of HIV RNA detection in reverse transcription quantitative polymerase chain reaction (RT-qPCR) has been enhanced.[65] Beacon probes tagged with dyes such as R6G, ROX, and Cy5 transitioned from dim aggregates to bright monomers upon hybridization or heating. Notably, ROX exhibited exceptional performance, surpassing even the Abbott Real-Time HIV-1 kit.[65] When tested in spiked human plasma and clinical samples from patients receiving highly active antiretroviral therapy (HAART), this method improved the detection of low-copy HIV RNA, thereby reducing the occurrence of false negatives.[65]

DNA and RNA can form various non-canonical structures, with the G-quadruplex (G4) being particularly notable (Fig. 3(A)).[72] This alternative DNA structure is characterized by its guanine-rich composition, stability, and polymorphism (Fig. 3(B)).[73] It plays a

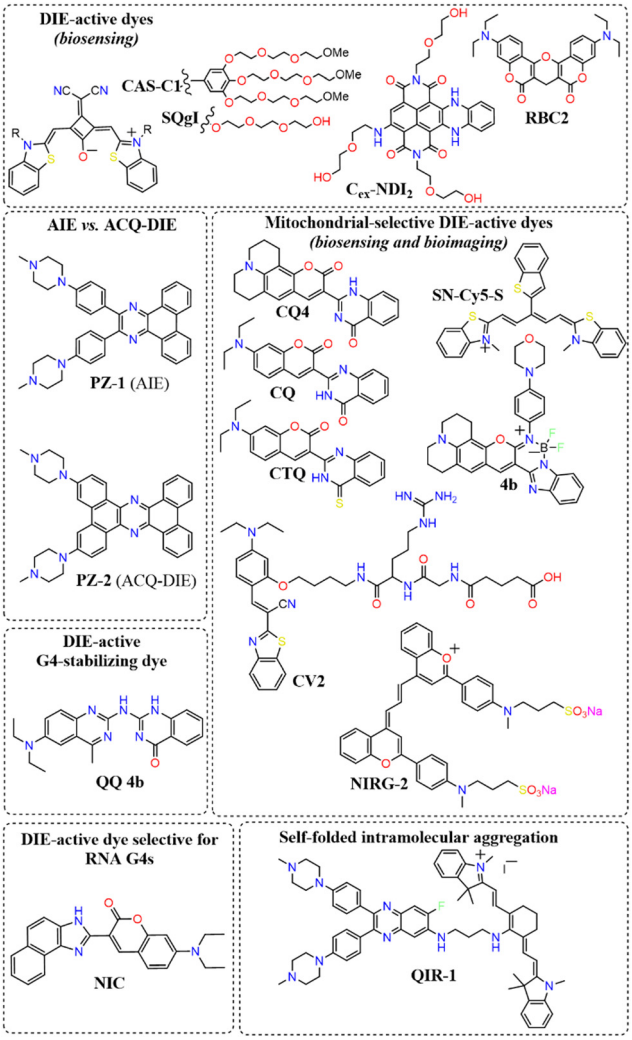

Scheme 1 Representative molecular structures of various DIE-active dyes targeting G4 structures.

significant role in cancer research due to its association with genomic instability.[74] Techniques like immunofluorescence, using the G4-specific antibody BG4,[75] and chromatin immunoprecipitation followed by sequencing (ChIP-Seq)[76,77] have enhanced our capacity to detect these structures within cells and chromatin. However, these methods only identify a portion of G4 sites. Imaging G4s in living cells remains challenging,[78,79] partially due to probe aggregation, which decreases the effectiveness of tracking these structures dynamically. These probes often employ hydrophobic chromophores to enhance selectivity for G4 over dsDNA, which may cause ACQ issues.[80] However, the interaction of these probes with G4 structures can lead to DIE, offering a solution to some of the challenges in fluorescence imaging and suggesting the possibility for real-time mapping of G4 structures (Fig. 3(C)).

A broad array of DIE-active dyes has been identified for detecting G4s in DNA or RNA, both in test tubes and within cancer cells. Specifically, dyes that function through DIE predominantly form intermolecular aggregates and target parallel G4 structures. This preference is due to the more accessible external tetrads found in parallel G4s, in contrast to the less accessible structures of hybrid and antiparallel G4 morphologies that incorporate lateral or diagonal loops (Fig. 3(B)).[82] Additionally, parallel G4s may form intermolecular structures that facilitate the disassembly of ACQ-based dyes. These dyes encompass various molecular structures, including squaraines,[33,60] core-extended naphthalene diimides,[83–85] coumarin[32,81,86–88]- and cyanine[89–91]-based dyes, boron-dipyrromethene (BODIPY) analogues,[62,92–94] quinazoline-quinazolinone derivatives,[61,95] and more[96–100] (Scheme 1).

In this context, Würthner and colleagues developed two near-infrared (NIR) fluorescent probes: amphiphilic dicyanovinyl-substituted squaraine dyes named **SQgI**[60] and **CAS-C1**.[33] These dyes were functionalized with triethylene glycol chains to enhance water solubility without altering the overall charge of the molecules, thereby promoting self-assembly likely driven by hydrophobic effects and/or dipole–dipole interactions among the squaraine scaffolds (Scheme 1).[16,101] In an aqueous environment, these probes tended to form non-emissive molecular aggregates with an H-type character (Fig. 3(D)). However, upon binding to biologically relevant parallel G4 structures, there was a notable increase in their photoluminescence quantum yields (Φ_F), with values of 0.61 for **SQgI** and 0.74 for **CAS-C1** (Fig. 3(D)).[33,60] Additionally, the interaction of **CAS-C1** with parallel G4 structures increased the dye's two-photon absorption cross-section (σ_2), with values ranging from 273 to 312 GM at 1275 nm, depending on the G4 structure it bound to (Fig. 3(E)).[33] This property enabled the **CAS-C1**:G4 complexes to function in a NIR-to-NIR mode, a highly requested configuration feature in nonlinear microscopy.

Ultrabright coumarin-quinazolinone dyes (**CQ**,[81] **CQ4**[32] and **CTQ**,[86] Scheme 1) designed for DIE have been reported to detect parallel G4 structures with high selectivity in both test-tube experiments and within cancer cells. Some of these dyes have proven to be effectively integrated not only in traditional confocal laser scanning microscopy[32,81] (CLSM, Fig. 3(F)–(H)) but also in advanced super-resolution bioimaging methods such as two-photon imaging[81] and stochastic optical reconstruction microscopy (STORM)[81] (Fig. 3(I)-(K)).

For this category of dyes, a carefully engineered design has also been utilized to minimize the background fluorescence of aggregates, aiming to develop absolute ACQ probes with a higher activation ratio upon binding to G4 structures, thereby achieving lower SBR. This has been demonstrated, for instance, by replacing oxygen atoms with sulfur atoms (**CTQ**,[86] Scheme 1), a structural modification also widely used in photodynamic therapy (PDT)[102–104] to enhance intersystem crossing.

Research has shown that fluorescence imaging in the NIR-II range (900–1700 nm) offers significant advantages over imaging in the NIR-I range (650–900 nm).[105–107] NIR-II imaging exhibits minimal autofluorescence and reduced photon scattering in living tissue, allowing for deeper penetration, higher resolution, and improved SBR. These benefits have garnered considerable interest for *in vivo* biological studies. In this context, Zhang and colleagues designed a cyanine derivative functionalized with two molecular rotor groups (**NIRG-2**, Scheme 1), demonstrating the capability to selectively detect

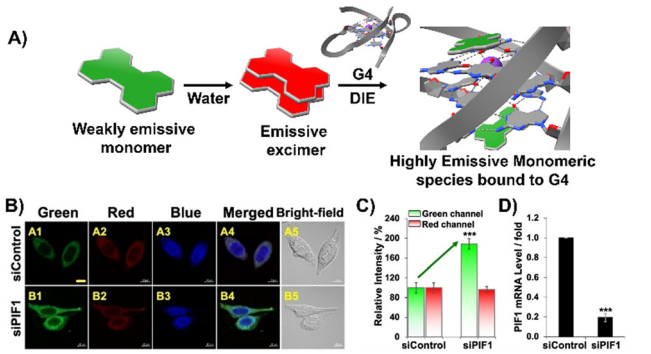

Fig. 4 (A) Schematic representation of the DIE operated by **CV2**. In aqueous environments, **CV2** tends to self-assemble into stable aggregates that exhibit excimer emission. Upon interacting with G4, these aggregates disassemble, shifting from red-emissive aggregates to green-emissive monomeric forms. (B) Investigating the impact of endogenous PIF1 knockdown on the fluorescence activation of **CV2** by DNA G4s in live HeLa cells, with DAPI used for nuclear staining. (C) Comparison of green and red fluorescence intensities in HeLa cells loaded with **CV2**, contrasting control with PIF1-silenced cells. (D) Assessment of PIF1 knockdown efficiency *via* quantification of PIF1 mRNA levels using RT-qPCR in both control and PIF1-silenced HeLa cells. Reprinted with permission from ref. 98. Copyright 2022 Wiley-VCH.

DNA G4s, providing a light-up response in the NIR-II window.[108] The molecules exhibited self-assembly properties in phosphate buffered saline (PBS), with an absorption band that was hypsochromically shifted. Upon complexation with a G4 structure, a potential disassembly occurred, reverting to a monomer-like absorption band and activating the fluorescence signal by halting the rotational movement of the rotor groups. **NIRG-2** had been effectively utilized to distinguish G4 structures *in vivo*, enabling the differentiation of tumours from normal tissues based on G4 abundance. Additionally, **NIRG-2** successfully tracked lymphatic metastasis in tumours through G4 detection.[108]

Diverging from the conventional intermolecular ACQ systems, DIE-active dyes that form excimer-emissive aggregates, which disassemble into highly emissive monomeric forms in the presence of parallel G4 structures, have also been developed (Fig. 4(A)). Specifically, Kim's group engineered a peptidyl fluorogenic probe named **CV2** (Scheme 1), combining a zwitterionic dipeptide receptor with a cyanovinylene dye linked by a tetramethylene linker.[98] CLSM and fluorescence lifetime imaging (FLIM) assessments confirmed **CV2**'s specificity for G4 structures, with its green monomeric fluorescence significantly diminished by Deoxyribonuclease I (DNase I) or competitive small-molecule G4 ligands. The probe's potential for monitoring G4 folding and unfolding dynamics was further demonstrated by inhibiting native helicases in HeLa cells, resulting in enhanced fluorescence (Fig. 4(B)–(D)). Furthermore, **CV2** proved effective in identifying mitochondrial DNA (mtDNA) damage, as cells exposed to DNA-damaging agents showed reduced **CV2** fluorescence, indicative of mtDNA depletion.[98]

Besides forming intermolecular aggregated structures, dyes active in DIE can also detect G4s through the disassembly of intramolecular aggregates, as demonstrated by compound **QIR-1** (Scheme 1).[89] However, to date, dyes working in this configuration for G4 detection are still limited,[109] and further work is needed to unlock their full potential.

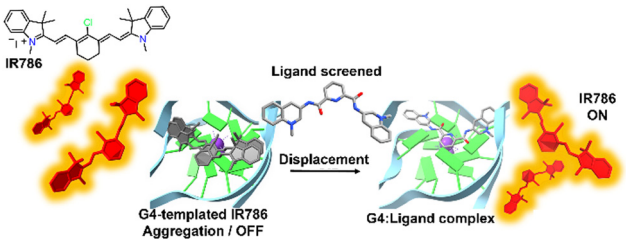

Fig. 5 Schematic illustration of the assembly of **IR786** to form H-aggregates on DNA G4. The emissive, isolated **IR786** binds to G4, forming non-emissive aggregates. Introduction of a high-affinity G4 ligand can displace **IR786** from the G4 template, restoring its fluorescence intensity.[110]

Aiming to enhance the drug-like properties of DIE-active probes, a quinazoline-quinazolinone derivative (**QQ 4b**, Scheme 1) has been developed.[61] This molecule not only displays selective fluorogenic light-up responses towards G4s upon disassembly but also shows sequence specificity. Furthermore, this agent has been demonstrated to inhibit DNA polymerase activity through the stabilization of G4 structures.

To date, the majority of dyes active in DIE are known to bind and sense DNA G4s. An exception is the molecule **NIC** (Scheme 1), which is capable of detecting and monitoring the dynamics of RNA G4s within cells.[87]

The DIE principle has been leveraged to create a supramolecular platform for the discovery of new G4-ligands. This technique departs from previous methods that rely on G4-induced dye disaggregation, instead using the self-assembly of the cyanine dye **IR786** on the G4 template.[110] **IR786** forms bright monomers, but in the presence of G4 structures, it transitions to dimly emissive aggregates, as illustrated in Fig. 5.[110] This change in optical properties upon interaction with G4s has led to the development of a turn-on fluorescence displacement assay, specifically designed to probe interactions between G4s and potential ligands. Introduction of a G4-ligand into the **IR786**:G4 mixture disrupts this aggregation, resulting in increased fluorescence from **IR786**. This innovative method offers a novel strategy for ligand screening and the identification of compounds that engage with G4 structures.

Recently, a direct comparison of G4 recognition capabilities was conducted between an AIE dye, **PZ-1**, and a DIE dye, **PZ-2** (Scheme 1).[97] These two molecules, which differ only in the size of their aromatic regions, demonstrated marked contrasts in performance. The DIE-active probe, **PZ-2**, significantly outperformed its AIE counterpart, **PZ-1**, which exhibited minimal changes in emission properties. Specifically, the DIE probe showed approximately 100-fold increase in fluorescence upon binding to G4 structures. This stark difference highlights the superior capability of the DIE-active probe in detecting G4 structures, offering both lower background emission and a more distinct switch-on fluorescence effect compared to its AIE counterpart.

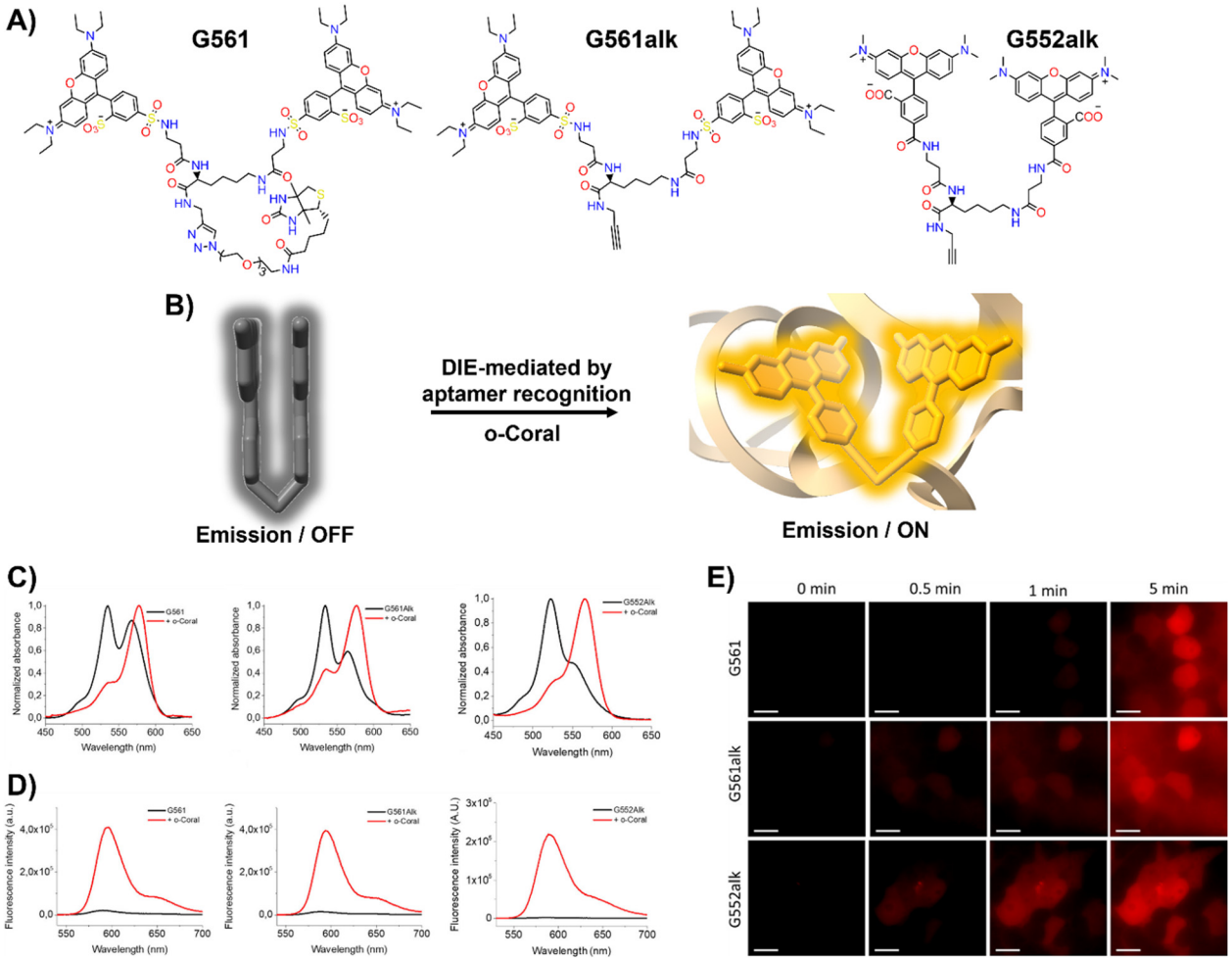

Fig. 6 (A) Chemical structures of intramolecularly formed self-assembled probes. (B) Concept of the fluorogenic response of self-quenched dyes upon aptamer binding. (C), (D) Absorption (C) and emission (D) spectra of **G561**, **G561alk** and **G552alk** in the absence and presence of *o-Coral*. (E) Fast detection of overexpressed *o-Coral*-tagged U6 RNAs in live cells with the fluorogens. Scale bars are 20 μm. Reprinted with permission from ref. 123. Copyright 2022 American Chemical Society.

3.2 RNA aptamers-mediated DIE

RNA is essential in numerous biological processes, and to understand its roles, scientists have devised various techniques for visualizing RNA molecules within cells.[111] Among these techniques are the fusion of RNA-binding proteins with fluorescent proteins,[112,113] and RNA-based fluorogenic modules[114] where bulky fluorescent proteins are replaced by smaller fluorogens.[115] A cutting-edge approach involves a semi-synthetic strategy that harnesses engineered RNA aptamers.[116–119] These aptamers are designed to specifically bind and activate the fluorescence of certain dyes, which are otherwise non-emissive until they interact with the aptamer. RNA aptamers are short, structured nucleotide sequences that can be engineered through a process known as the systematic evolution of ligands by exponential enrichment (SELEX).[120,121] This method fine-tunes their ability to recognize specific dyes with remarkable precision, enhancing their affinity for fluorogenic dyes.

Despite advancements in this field, the practical application of dye-aptamer systems has been limited by the dyes' brightness and stability under light.[122]

In response to this limitation, the Klymchenko group developed a novel dye known as **Gemini-561** (**G561**), which utilizes sulforhodamine B (SRB) linked dyes through an innovative approach based on intramolecular dimerization-caused quenching (DCQ) of fluorescence (Fig. 6(A) and (B)).[34] This method allows for the use of lower concentrations of the probe while significantly enhancing the SBR. Through a combination of genetic engineering and selective processes, RNA aptamers were specifically designed to bind this dye, yielding a notable variant named *o-Coral*.[34] This binding interaction, with a dissociation constant of 73 nM, disrupted the aggregated state of **G561**, triggering a 13-fold increase in fluorescence (Fig. 6(C) and (D)).[123] *o-Coral* was capable of forming a bright complex with **G561**, distinguishing itself by its ability to directly visualize specific RNA molecules in mammalian cells without the need for multiple tagging.[34,123] This system represented a significant leap in RNA imaging, offering a powerful tool for observing RNA molecules in their natural cellular context with unprecedented clarity and specificity.

Further evaluations of chemical modifications and enhancements to **G561** resulted in the development of two dyes: the

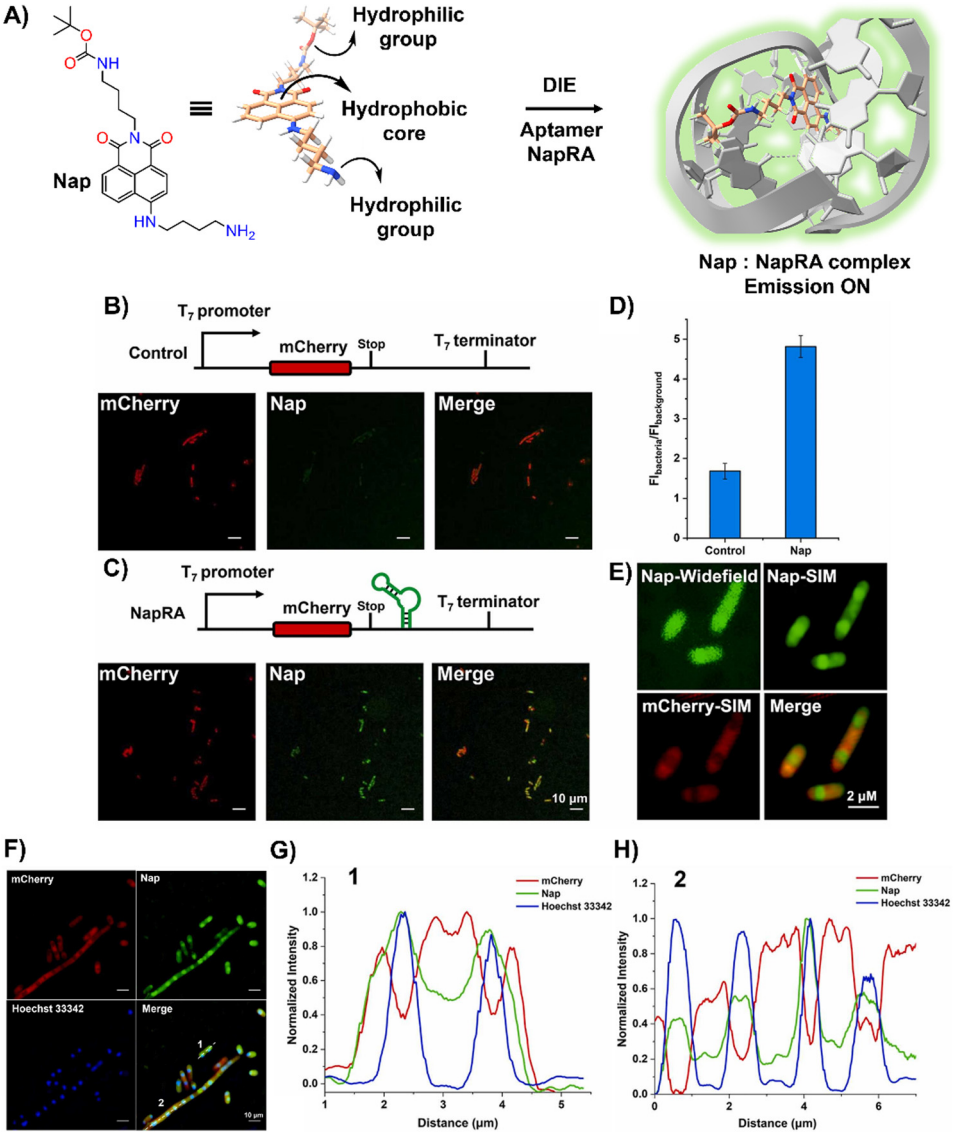

Fig. 7 (A) Schematic illustration of the strategy based on the aggregation–disaggregation of **Nap** for RNA labelling. (B) Expression scheme of control mCherry mRNA and no-wash confocal imaging in bacteria using **Nap**. (C) Expression scheme of mCherry-*NapRA* mRNA and no-wash confocal imaging with **Nap**. (D) Ratio of **Nap** fluorescence intensity in bacteria expressing mCherry-*NapRA* mRNA compared to the control. (E) Widefield and SIM imaging of *E. coli* expressing mCherry-*NapRA* mRNA treated with **Nap**. (F) SIM imaging of *E. coli* expressing mCherry-*NapRA* mRNA treated with **Nap** and Hoechst 33342. (G) Normalized intensity profile along dotted line 1 in (F). (H) Normalized intensity profile along dotted line 2 in (F). Scale bar: 10 μm. Reprinted with permission from ref. 124. Copyright 2023 Elsevier.

non-biotinylated **Gemini-561-alkyne** (**G561alk**) and its closely related analogue, **Gemini-552-alkyne** (**G552alk**) (Fig. 6(A)).[123] The latter features a carboxylate group in place of a sulfonate and dimethylamino groups instead of diethylamino. It demonstrated a remarkable 111-fold enhancement in fluorescence and an increased affinity constant of 7.5 nM for *o-Coral* (Fig. 6(C) and (D)).[123] These refinements resulted in even greater sensitivity and brightness in RNA imaging applications, enabling effective detection of *o-Coral*-tagged RNAs in live cells (Fig. 6(E)).[123]

Parallel to these developments, Xu and colleagues reported on a naphthalimide-based fluorophore, **Nap**, which self-assembled into nanoparticles for RNA imaging (Fig. 7(A)).[124] By binding with a guanine-rich RNA aptamer, *NapRA*, **Nap**'s fluorescence was enhanced, enabling the visualization of mCherry mRNA in *E. coli*. Integrating *NapRA* into mCherry's 3′-untranslated region did not affect gene expression or protein functionality but allowed for the selective illumination of cells expressing mCherry-*NapRA* (Fig. 7(B)–(D)).[124] The study also utilized structured illumination microscopy (SIM) for super-resolution imaging, pinpointing mRNA locations within bacterial cells, particularly around the nucleoid area (Fig. 7(E)–(H)).[124] This aligned with findings on mRNA distribution and suggested that newly transcribed mRNA first appeared near the nucleoid, potentially moving to the periphery later.

3.3 DNA-mediated disaggregation in the context of phototherapeutics

DNA-driven molecular disassembly has been utilized to impart stimuli-responsiveness to materials with phototherapeutic and

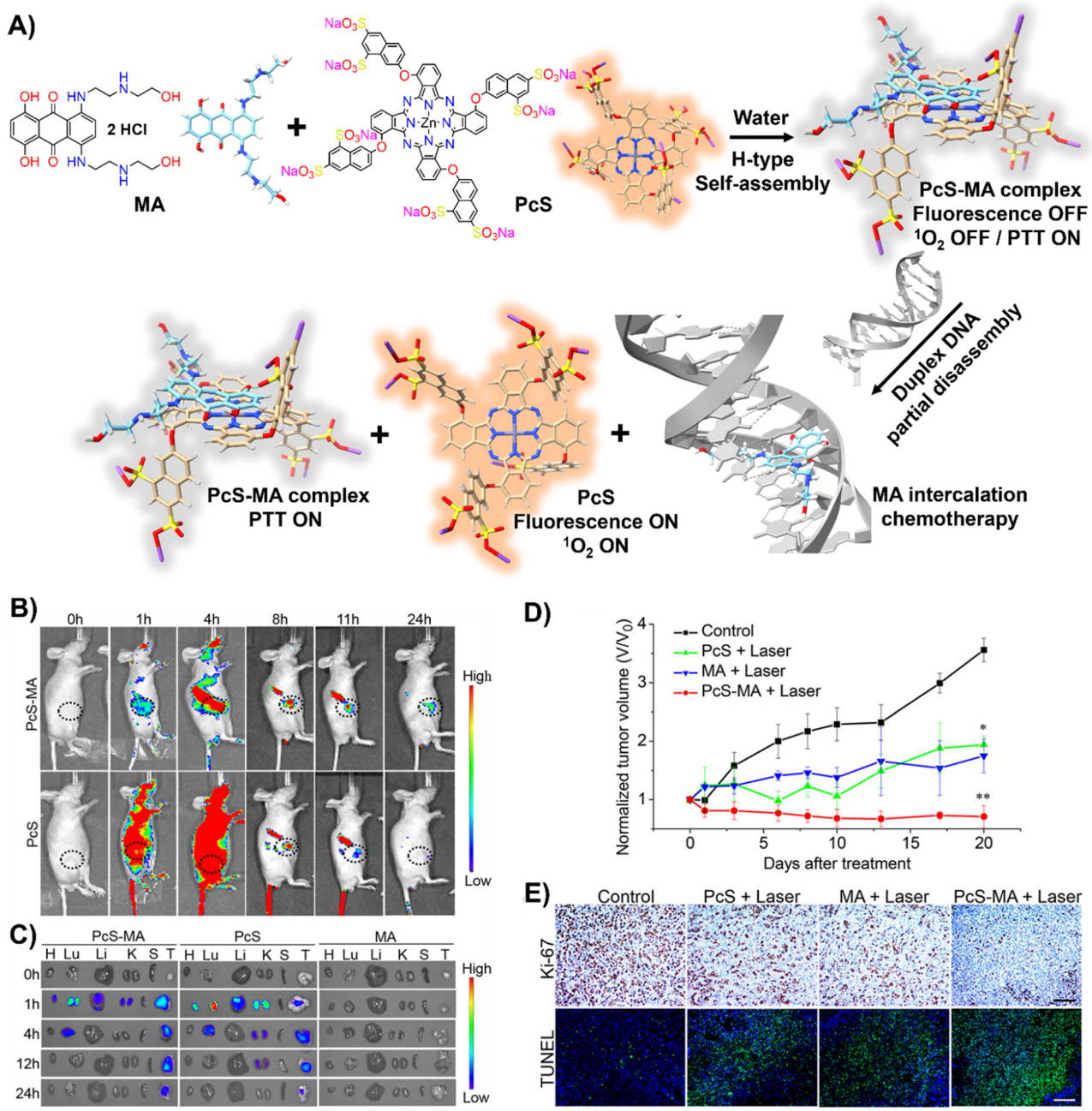

Fig. 8 (A) Schematic illustration of a nanotheranostic agent constructed *via* supramolecular interactions between **PcS** and **MA**, featuring nucleic-acid-driven activatable properties for enhanced fluorescent imaging, PDT, PTT, and synergized chemotherapy. (B) and (C) *In vivo* and *ex vivo* fluorescence imaging of tumour-bearing mice before and after intravenous injection of **PcS-MA**, **PcS**, and **MA**. (B) MCF7 tumour model: tumour sites are highlighted with dotted circles. (C) SW620 tumour model: labels—H for heart, Lu for lung, Li for liver, K for kidney, S for spleen, T for tumour. (D) Phototherapeutic efficacy of **PcS**, **MA**, and **PcS-MA** in mice with MCF7 tumours. (E) Histological examination of MCF7 tumours on day 21 post-treatment. Proliferation detected with Ki-67 antibody (brown signals), and nuclei counterstained with hematoxylin. Apoptosis was assessed by TUNEL assay (positive signals in green), with nuclei stained by DAPI (blue). Scale bars: 50 μm for Ki-67 images, 100 μm for TUNEL images. Reprinted with permission from ref. 126. Copyright 2018 American Chemical Society.

chemotherapeutic properties. Specifically, ACQ effects are widely recognized for their significant limitations on activating dyes, such as in PDT for the generation of reactive oxygen species (ROS).[15,125]

In this field, Yoon and colleagues showcased the spontaneous formation of complexes between the water-soluble photosensitizer (PS), zinc(II) phthalocyanine tetrasubstituted with 6,8-disulfonate-2-naphthyloxy groups (**PcS**), and the renowned anticancer drug, mitoxantrone (**MA**), leading to the creation of uniform **PcS-MA**-based nanoparticles (Fig. 8(A)).[126]

These nanoparticles formed H-type non-emissive aggregates, which, while unable to generate singlet oxygen ($^1O_2$),

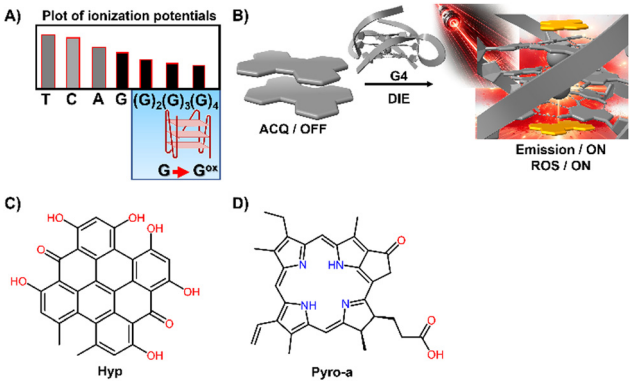

Fig. 9 (A) Plot of ionization potentials showing that guanine has the lowest potential, making guanine-rich sequences particularly susceptible to oxidation. (B) Schematic representation showing how a G4 mediates the disassembly of ACQ-active dyes, restoring their fluorescence properties and facilitating the generation of ROS. (C) and (D) Chemical structures of **Hyp** and **Pyro-a**.

retained their intrinsic photothermal capabilities (PTT). The introduction of duplex DNA into the binary system facilitated the intercalation of **MA**, driving the disassembly of the **PcS-MA** complex and restoring the fluorescence intensity and the photosensitization efficiency of **PcS**. The absence of interference from metal ions and proteins underscored the system's specificity for DNA recognition. *In vivo* and *ex vivo* studies showed that **PcS-MA** nanoparticles accumulated efficiently in tumour tissues of mice, and laser irradiation significantly reduced tumour growth and induced apoptosis (Fig. 8(B)–(E)).

G4 DNA and RNA structures, characterized by their guanine-rich regions, are particularly susceptible to oxidation due to the electron-rich nature of guanine, which is the most oxidation-prone of the DNA bases (Fig. 9(A)).[127–129] This susceptibility is heightened in G4 structures, where the guanine bases are π-stacked, effectively lowering their ionization potential and rendering them more vulnerable to oxidative processes. As a result, G4 structures are acutely responsive to ROS, making them focal points for PSs.[130–134] Recent studies have shown that self-assembled inactive PSs, upon binding to G4 structures, can disassemble and catalyse the production of ROS, potentially causing DNA damage (Fig. 9(B)).[135,136]

For example, the interaction of DNA G4s with Hypericin (**Hyp**), a polycyclic quinone extracted from Hypericum possessing antiviral and anticancer activities, has been shown to amplify its photosensitizing effects upon DIE (Fig. 9(C)).[135] The efficiency of $^1O_2$ quantum yield (Φ_Δ) in the complex formed with the *c-KIT* G4 structure in water was notably high at 0.67, underscoring the significance of these interactions in a biologically relevant medium.

Similarly, Pyropheophorbide a (**Pyro-a**), a derivative of chlorophyll known for its efficacy as a PS, demonstrated increased fluorescence and photosensitizing efficiency upon binding to parallel G4 structures (Fig. 9(D)).[136] These observations highlight the critical role of preventing dye aggregation to boost the biosensing capabilities and phototherapeutic applications of ACQ dyes and other inactive materials.

Although this research area is still in its infancy, the strategic targeting of cancer-associated molecules with such innovative approaches heralds promising developments in phototherapy.

3.4 Serum proteins-mediated DIE

Human serum albumin (HSA) is an important thiol-containing protein found in blood and urine, with plasma concentrations typically ranging from 35 to 50 g L^{-1}, and urine levels under 30 mg L^{-1}.[137,138] HSA is essential for regulating plasma colloidal osmotic pressure and facilitating the transport of various substances.[139,140] Notably, HSA plays a significant role in tumour nutrition, possibly due to the overexpression of albumin receptors and albumin-binding proteins on cancer cells, which promotes albumin accumulation and degradation in tumour tissues.[141] The rapid diagnosis of changes in HSA concentrations in body fluids is thus of clinical importance.[142,143] Researchers have explored the DIE concept, leveraging albumin's capacity to bind hydrophobic self-assembled molecules and convert them into highly monomeric species. To date, compounds like squaraine,[140,142,144] BODIPY,[145–149] coumarin,[138,150] chalcone,[151] and cyanine[152,153] have been used for both qualitative and quantitative biosensing of serum albumin proteins (SAP) *in vitro* and *in vivo*.

Most studies apply the DIE concept directly to target SAP in blood samples,[154] using noncovalent interactions between ligand aggregates and albumin (Fig. 10(A)). This approach utilizes molecules with enhanced hydrophobic surfaces to improve aggregate stability in protic solvents through π–π and C–H···π interactions, enhancing their interaction with the protein's hydrophobic cavities.[153–155] The molecules have been specifically designed to exhibit selectivity towards HSA over other biomolecules[156] like DNA, RNA, pepsin, and trypsin, with detection limits typically ranging from 1 to 140 nM.[154,157] Furthermore, site-specific binding probes not only detect HSA in bodily fluids but also monitor changes in the protein's conformation and enable fluorescence imaging of SAP in living cells, demonstrating the versatility of HSA probes.[154,157]

Yoon and colleagues demonstrated the specific binding of an exogenous probe, composed of zinc(II) phthalocyanine mono-α-substituted with 4-sulfonatophenoxyl (**PcS**), to albumin *in vivo* (Fig. 10(A)).[158] This was accomplished using a transgenic mouse system, where albumin was tagged with yellow fluorescent protein (YFP) through intraperitoneal injections of tamoxifen. **PcS** aggregates were administered intravenously, and plasma analysis one hour post-treatment showed that the aggregates were trapped and disassembled by albumin. Confocal imaging of liver and lung sections from treated mice revealed overlapping fluorescence between **PcS** and albumin-YFP. This method provides a valuable technique for tracking specific proteins *in vivo* systems.

Another strategy involves forming a covalent bond between the squaraine-based probes (**Sq**[142] or **SQSS**[140]) and the serum protein (Fig. 10(B)). In this method, the probe is engineered with a thiol-sensitive motif, enabling it to react with the cysteine (Cys) residues of SAP. The interaction proceeds

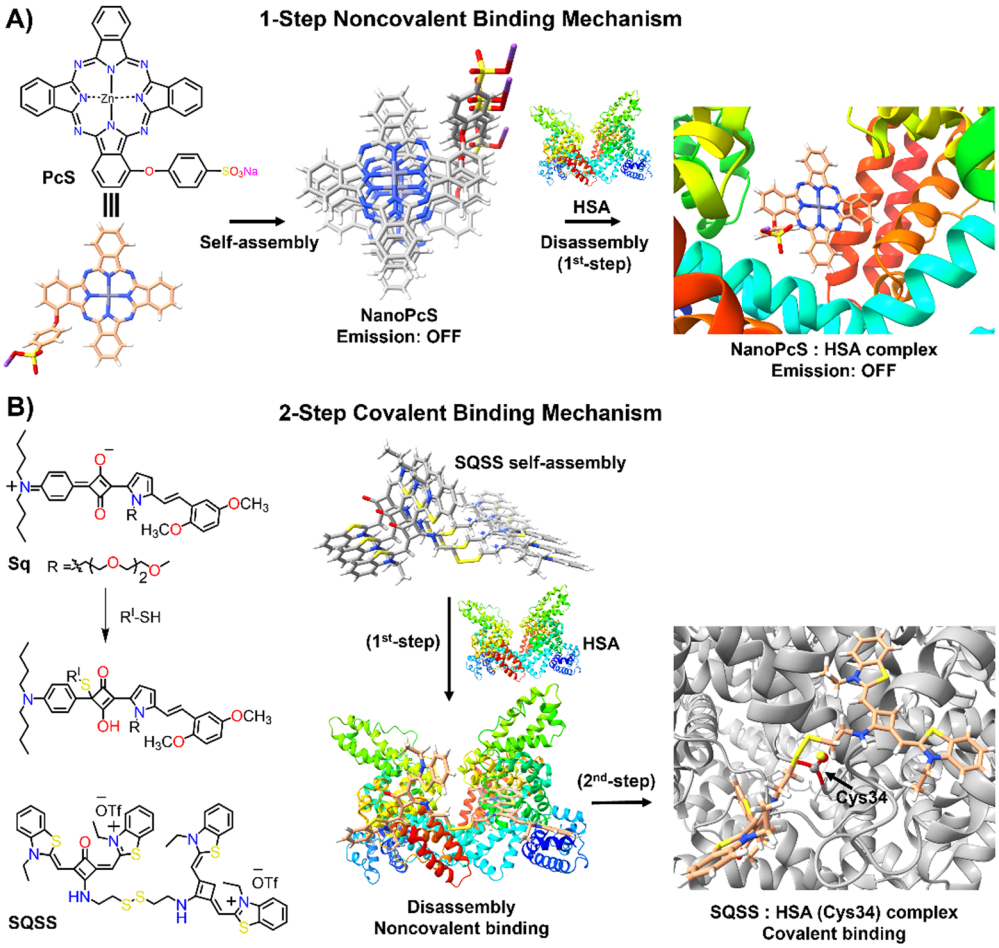

Fig. 10 Schematic representation of the molecular recognition mechanisms mediated by DIE-active dyes for detecting HSA. Panel (A) shows the noncovalent binding approach, exemplified by the molecule **PcS**,[158] used to sense HSA. The self-assembled structure of **PcS** gradually disassembles in the presence of HSA through a one-step mechanism. Panel (B) depicts the covalent binding approach, illustrated by the molecules **Sq**[142] and **SQSS**.[140] In an aqueous solution, **SQSS** molecules self-assemble. Upon encountering HSA, a two-step binding process begins with an initial noncovalent binding mechanism, which is then followed by a selective covalent binding. This second step is driven by a thiol-sensitive motif and the Cys34 residue of HSA.

through a two-step mechanism: initially, compact probe assemblies loosen *via* noncovalent interactions, followed by gradual disassembly driven by the presence of Cys34 in SA through covalent binding. This results in a newly formed chromophore that emits a strong fluorescent signal with high selectivity towards SAP over other thiol-containing proteins, achieving detection limits as low as 0.53 nM.[140] It is noteworthy that the covalent binding to Cys34 may involve a base-catalysed nucleophilic addition, which restricts its practical use to basic conditions (pH $\sim$ 8).[142]

Laboratory testing is generally required to detect HSA. However, there is a critical need for point-of-care (POC) monitoring of HSA, particularly for elderly or chronically ill patients, as low levels of HSA—a condition known as hypoalbuminemia---indicate disease states such as hepatic impairment, chronic kidney disease, protein-losing enteropathy, burns, and sepsis.[159,160] In response, Liu and colleagues designed a 2′-hydroxychalcone derivative named **4MC**, capable of detecting HSA through the DIE process (Fig. 11(A)).[151] **4MC** formed excimer-emissive aggregates that disassembled into highly emissive monomeric forms in the presence of HSA. The concentration of HSA was determined by the emission ratio of aggregated to monomeric probes, resulting in visually distinct red and green colour changes (Fig. 11(B) and (C)). As a proof of concept, a microfluidic paper-based analytical device (μPAD) was integrated with **4MC** to create a POC device for HSA detection in whole blood. This μPAD featured an outer layer of plasma separation membrane and a detection pad constructed from wax-patterned filter paper impregnated with **4MC**. Demonstrations showed that such a device could be effectively used at home, with HSA levels assessable using a UV lamp for excitation and a smartphone for detection (Fig. 11(D)–(G)). The glowing spots on the paper device could be captured by the smartphone's camera and directly analysed using a dedicated app to provide RGB values.[151]

3.5 Membrane proteins-mediated DIE

Membrane proteins, which are associated with or attached to cellular membranes or within cell compartments or organelles, play pivotal roles in functions such as molecule transport, cell signalling, cell adhesion, and pathogen recognition.[161,162] In

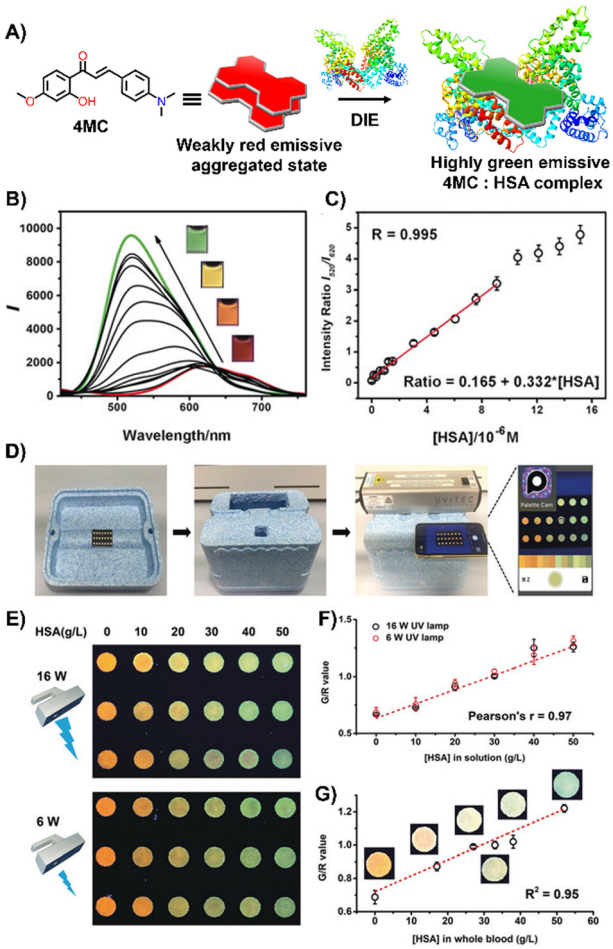

Fig. 11 (A) Chemical structure and ratiometric detection method of **4MC** for HSA. (B) and (C) Fluorescent spectra (B) and the intensity ratios (I_{520}/I_{620}, monomer/aggregate) (C) of **4MC** in response to increasing concentrations of HSA in water. The inset shows photographs under UV irradiation (365 nm) with varying concentrations of HSA. (D) Setup of the mobile-phone-based testing system. (E) Photograph of test paper used to analyse aqueous HSA solutions at increasing concentrations, excited by different handheld UV lamps (16 W and 6 W power, 365 nm). (F) and (G) Calibration curves for aqueous HSA solutions (F) and whole blood samples (G), respectively. Reprinted with permission from ref. 151. Copyright 2020 Wiley-VCH.

this context, the development of protein-targeting probes that enable real-time, highly selective imaging of protein dynamics is of significant importance for diagnosing various diseases, including cancer.[163,164]

A variety of dyes sensitive to protein membranes have been identified.[161,165–167] One of the pioneering efforts in this area was led by Hamachi and colleagues, who developed a self-assembled supramolecular ligand-tethered probe (**1**, Scheme 2) to visualize folate receptors in KB cells, observing robust fluorescence on the cell surface.[168]

Subsequently, Tan and co-workers designed a near-IR fluorogenic Cy5 probe with a benzenesulfonamide ligand (**Cy5-1**, Scheme 2) targeting human carbonic anhydrase (hCA).[169] In PBS buffer, the probe forms a self-assembled aggregate with a Φ_F of 0.019. The presence of hCAII protein

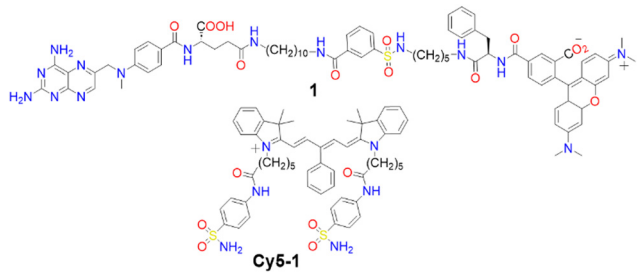

Scheme 2 Chemical structures of compound **1** and **Cy5-1**.

triggers disassembly, resulting in an increased Φ_F of approximately 0.28, with a LOD of 17 nM. **Cy5-1** was used to image HeLa cells known for overexpressing hCAIX on the extracellular surface under hypoxic conditions. Live-cell imaging with CLSM revealed intense surface fluorescence, illustrating **Cy5-1**'s capability to detect changes in the hypoxic environment of cancer cells.

To enhance the drug-like properties of DIE-active probes, Nesterov and colleagues developed phthalocyanine-based sensors specific for the epidermal growth factor receptor (EGFR), with exceptionally low LODs of 3 nM[165] and 2 nM.[167] These probes selectively label EGFR tyrosine kinase inside cells, making them suitable for selective fluorescent imaging of the protein in both fixed and live cells.[167]

Stimuli-responsive dyes have also been employed for imaging protein membranes, using the DCQ mechanism.[162–164,170] This strategy, pioneered by Klymchenko's research team, was used to image the oxytocin receptor,[64,162] the biotin receptor,[163] and $\alpha_v\beta_3$ integrin[170] in both *in vitro* settings and live cells. The successful cellular visualization of membrane proteins with specially designed probes prompted Klymchenko and Bonnet to explore this approach further for visualizing the naturally expressed oxytocin receptor in living mice using a specially designed probe, Cy5.5 decorated with a PEG linker and the peptidic carbetocin (**CBT**) ligand (**dCy5.5-PEG–CBT**, Fig. 12(A) and (B)).[64] The probe was intravenously administered to lactating Swiss mice, and imaging showed visualization of the mammary glands and liver with specificity superior to that of the monomeric probe **mCy5.5-PEG-CBT** (Fig. 12(C)–(F)).[64]

In light of these findings, Qian and colleagues implemented the DCQ strategy for real-time imaging of the EGFR receptor with antibody-based fluorogenic probes.[171] Cellular studies on A431 ($EGFR^+$) and HepG2 ($EGFR^-$) cells showed intense fluorescence on the former, indicating excellent selectivity. Live-cell imaging demonstrated intracellular fluorescence signifying internalization of the antibody–EGFR complex. Furthermore, fluorescence-activated cell sorting allowed for quantitative analysis of endogenous EGFR expression levels in A431 cells, revealing a linear relationship between fluorescence intensity and probe concentration.[171]

3.6 Proteins-mediated disaggregation in the context of phototherapeutics

Molecular probes that possess both DIE and photosensitizing properties, and that target overexpressed or cancer-promoting proteins, represent a novel approach in activatable PDT to enhance treatment selectivity.[103,104,172,173] This section

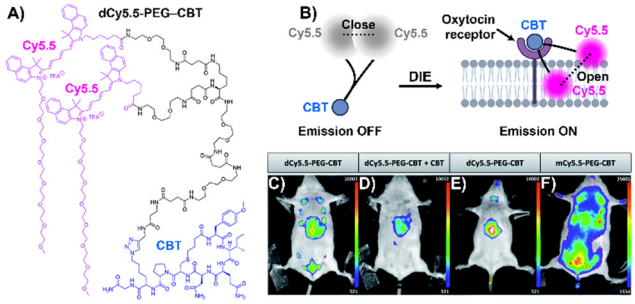

Fig. 12 (A) Chemical structure of **dCy5.5-PEG-CBT**. (B) Recognition mechanism mediated by **dCy5.5-PEG-CBT**. (C)–(F) *In vivo* images of lactating mice (C), (D), and (F) and a naïve mouse (E) injected intravenously *via* the tail with 7.5 nmol of **dCy5.5-PEG-CBT** (C) and (E), 7.5 nmol of **dCy5.5-PEG-CBT** along with 450 nmol of **CBT** (D), or 7.5 nmol of **mCy5.5-PEG-CBT** (F), taken 30 minutes prior to imaging. Reproduced from ref. 64 with permission from the Royal Society of Chemistry.

discusses three distinct strategies that have been employed so far (Fig. 13).

The first strategy involves the direct disaggregation of the PS in the presence of targeted proteins which leads to increased Φ_F and Φ_Δ (Fig. 13(A)).[102,158,173–176] The structural modification of PSs with specific anchor groups allows targeting of particular proteins. For example, using the folate receptor enhances the cellular uptake of folate-porphysome into cancer cells.[174] When combined with laser treatment, this method partially inhibited tumour growth.[174] Additionally, developed phthalocyanine derivatives, modified with anchor groups such as biotin (**Pc-4TEG-B**,[173] **PC-VH**[175]) to target the biotin receptor or sulfonate derivatives (**PcS**,[158] **PcS-4**[177]) to target albumin, were administered to tumour-bearing mice (Scheme 3). Light irradiation led to approximately 40% tumor growth inhibition with **Pc-4TEG-B**,[173] 55% or 85% with **PcS-4**,[177] **PC-VH**[175] respectively, and even complete inhibition and reduction in tumour volume with **PcS**[158] treatment.

The second strategy utilizes a drug carrier system to deliver the ligand to specific sites (Fig. 13(B)). Yoon and colleagues designed a system using mesenchymal stem cells (MSCs),

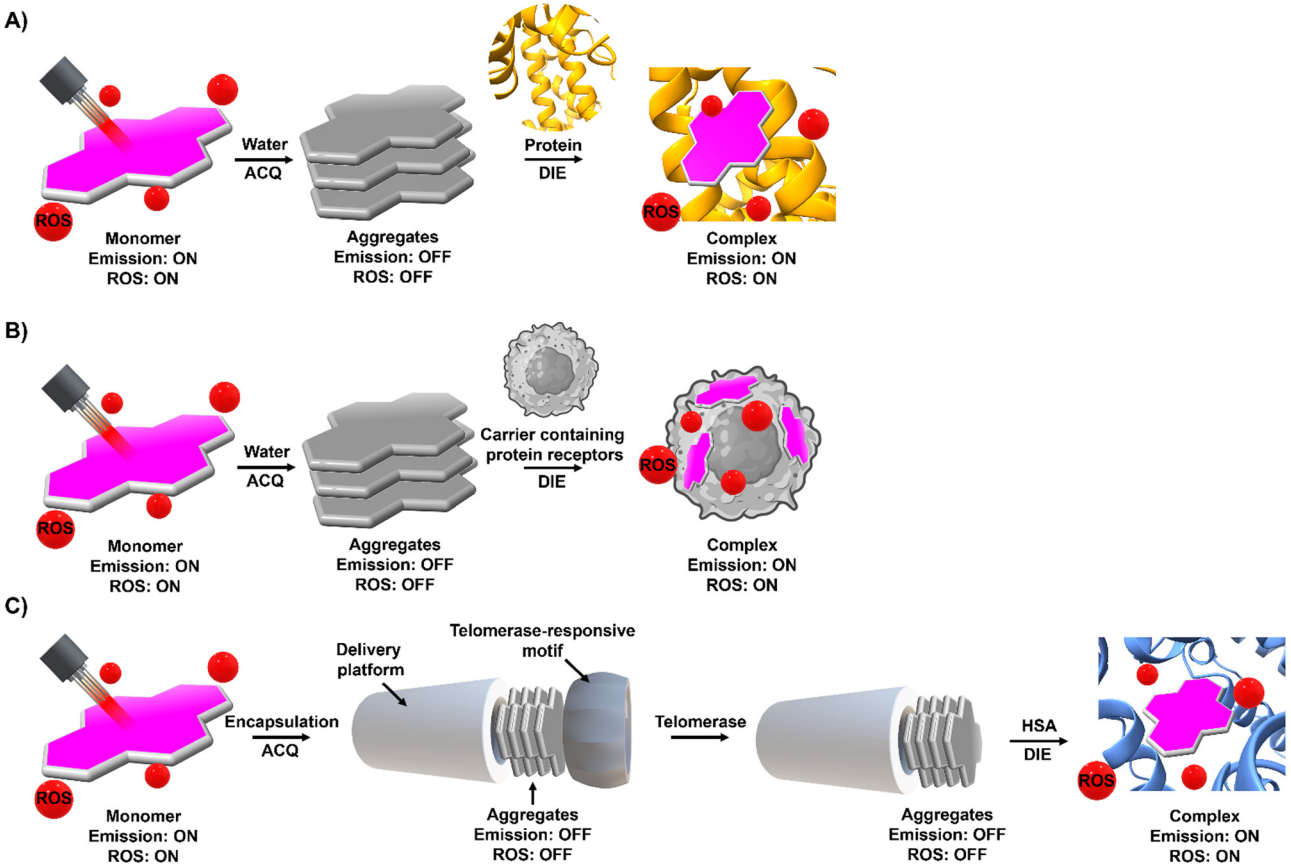

Fig. 13 Phototherapeutic strategies used by DIE-activated PSs coordinated with proteins. (A) In its monomeric form, typically found in organic solvents, the PS is photoactive. However, transitioning to an aqueous environment leads to the formation of molecular aggregates, causing a loss of photosensitization capability. Binding to a protein can restore the PS to a monomer-like state, reactivating its ROS production. (B) Similarly to (A), in an aqueous solution, the PS forms molecular aggregates that inhibit its photosensitization properties. Encapsulating the PS in a biological matrix containing proteins disperses the PS into a monomeric form, thereby restoring its ROS production capability. Once encapsulated within the matrix, the PS can be utilized as a delivery system. (C) The PS is encapsulated within an artificial delivery platform that initially quenches its photosensitizing properties, further secured by a protein-responsive motif, such as a DNA sequence. Interaction with specific triggers, in this case telomerase and HSA, leads to the elongation of the DNA sequence and the opening of the delivery platform. This allows direct interaction with HSA, forming a well-defined complex with the PS that restores its monomeric form and ROS production capability.

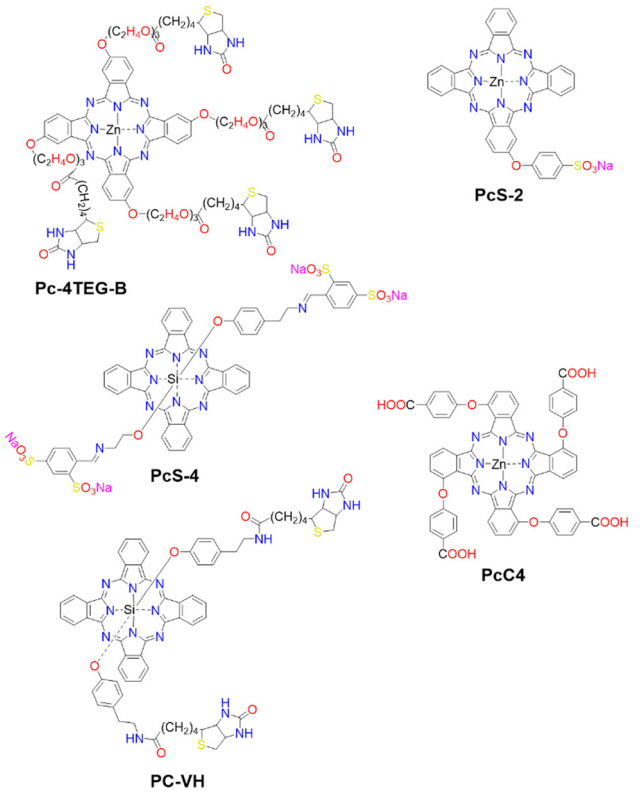

Scheme 3 Molecular Structures of PSs employing various mechanisms: **Pc-4TEG-B**, **PcS-4**, and **PC-VG** function through noncovalent interactions (refer to Fig. 13(A)). **PcS-2** is embedded within a cell-based drug carrier (see Fig. 13(B)), and **PcC4** is encapsulated in a drug delivery platform responsive to two protein triggers (see Fig. 13(C)).

which naturally possess tumour tropism mediated by growth factors,[178] combined with a phthalocyanine derivative (**PcS-2**,[179] Scheme 3) that forms H-type aggregates in water. After internalization of **PcS-2** by MSCs and subsequent spontaneous disassembly of the aggregates in the presence of albumin, the complex was intraperitoneally administered to HCT116 tumour-bearing mice.[179] This resulted in targeted accumulation in the tumour compared to the broader distribution of **PcS-2** alone in the abdomen. Irradiation with a 655 nm laser triggered the PDT mechanism, resulting in a 37% inhibition of tumour growth in mice treated with MSC-**PcS-2**.[179]

The third strategy aims to enhance tumour specificity and minimize side effects by targeting two cancer-related proteins (Fig. 13(C)).[180] This approach involved a sequentially activated, protein-responsive PS, based on a zinc(II) phthalocyanine derivative (**PcC4**, Scheme 3) entrapped in mesoporous silica nanoparticles (MSNs), with wrapping DNA (O1) serving as a biogate.[180] The **PcC4-MSN-O1** system exhibited self-quenching photoactivity, which was dramatically activated in sequence by telomerase and then albumin. Cellular studies demonstrated selective phototoxicity towards cancer cells with overexpressed telomerase.[180] Furthermore, the administration of **PcC4-MSN-O1** with light irradiation to HeLa tumour-bearing mice led to the inhibition of tumour growth, without showing any pathological changes in the mouse tissues, thereby demonstrating both the effectiveness and biocompatibility of this approach.[180]

3.7 Lipids-mediated DIE

Lipids, encompassing fatty acids, glycerolipids, glycerophospholipids, sphingolipids, and sterols, are vital for various cellular functions and as disease indicators for conditions like tumours and cardiovascular issues.[181–187] Fatty acids are essential for energy, cell structure, and signalling;[188] sphingolipids and glycerophospholipids for membrane structure;[189,190] and steroids, such as progesterone and cortisol, for regulating reproduction[191] and immunity.[192] Despite their significance, the efficient detection and imaging of lipids and steroids in biological settings continue to be a challenge.[193] Up to now, several DIE-active dyes sensitive to lipids have been reported, with some examples highlighted in this and the following sections.[29,35,63,194–202]

Jiang and colleagues developed a molecular probe, **IR1061**, for *in vivo* imaging of lipids in fatty liver diseases,[203] leveraging the DIE process.[194] In organic solvents, **IR1061** emitted brightly in the NIR-II region but remained non-fluorescent in aqueous environments due to ACQ (Fig. 14(A)). The probe's fluorescence was activated in PBS with DSPE-PEG2000 liposomes, indicating disaggregation and maintaining stability and specificity under various conditions.[194] *In vivo* experiments using atherosclerosis (AS) models (apolipoprotein E knock-out, ApoE$^{-/-}$ mice on a high-fat diet) and healthy C57bl/6 controls showed that only AS mice exhibited a significant, time-dependent increase in liver fluorescence, unlike other organs or controls (Fig. 14(B) and (C)).[194] A similar pattern was observed in an obesity (OB) model, where **IR1061** specifically highlighted lipid accumulation in the livers of OB mice (Fig. 14(D) and (E)).[194] These findings demonstrated **IR1061**'s potential as a DIE-based tool

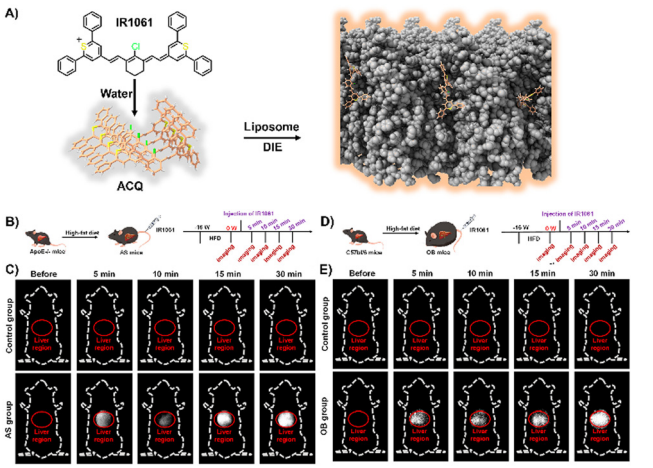

Fig. 14 (A) Schematic illustration depicting the use of lipid-activated IR1061 for imaging in AS and OB mouse models. (B) Development of the AS model. (C) Fluorescence imaging comparing the control and AS groups before and after IR1061 injection. (D) Development of the OB model. (E) Fluorescence imaging of the control and OB groups before and after IR1061 injection. Reprinted with permission from ref. 194. Copyright 2024 American Chemical Society.

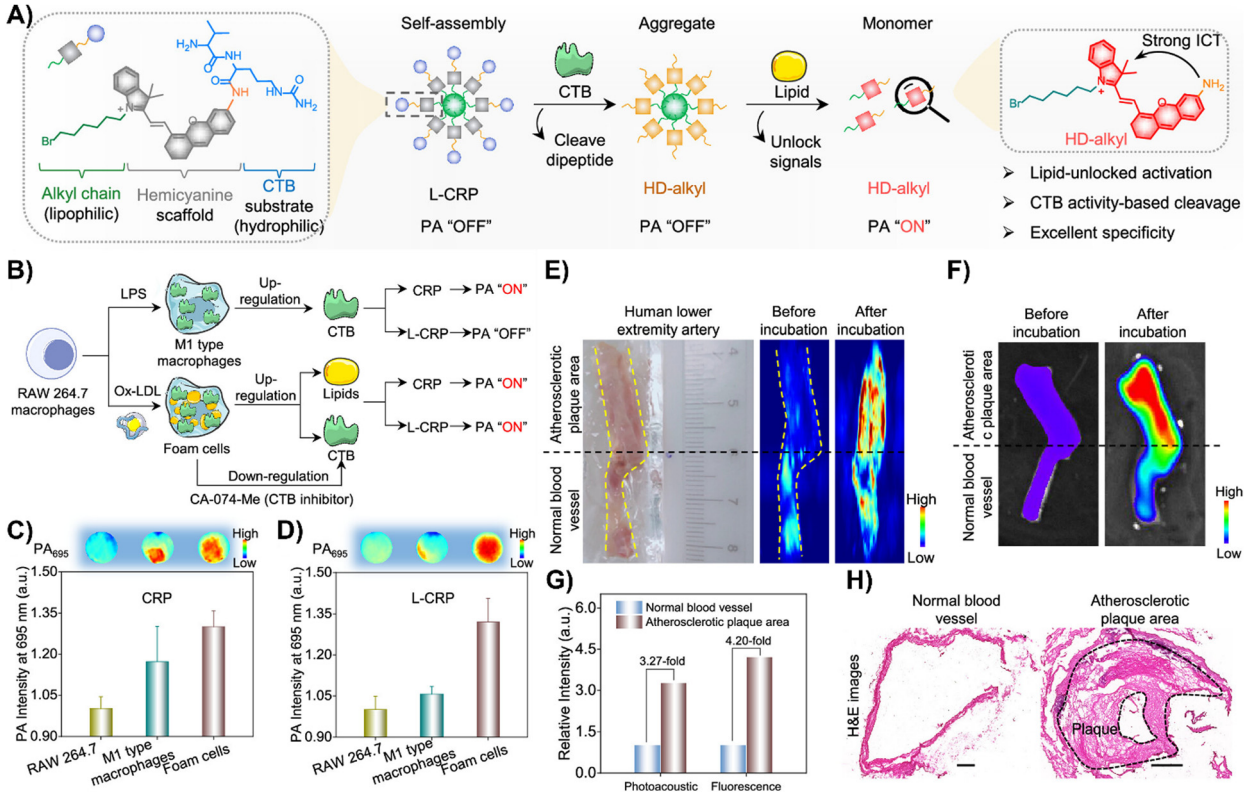

Fig. 15 (A) Chemical structure and activation mechanism of the lipid-unlocked CTB-responsive probe (**L-CRP**): composed of a hydrophilic CTB-responsive dipeptide, a lipophilic alkyl chain, and a caged hemicyanine unit, **L-CRP** aggregates in hydrophilic environments both before and after CTB incubation. In lipophilic environments, CTB recognition triggers the release of HD-alkyl as a monomer. (B) Construction of M1-type macrophages and foam cells: LPS induces M1-type macrophages with increased CTB expression. Ox-LDL causes foam cells to upregulate lipids and CTB, while the CTB inhibitor CA-074-Me decreases CTB levels in foam cells. (C) and (D) Photoacoustic intensity of **CRP** and **L-CRP** after various treatments, with insets showing PA images at 695 nm. (E) Bright field and PA imaging of a human lower extremity artery before and after **L-CRP** incubation in CTB buffer. The yellow dotted curves outline the blood vessel; the black dotted line marks the boundary between atherosclerotic plaque (above) and normal vessel (below). (F) Fluorescence imaging of the human lower extremity artery pre and post **L-CRP** incubation. (G) Quantitative analysis of PA and fluorescence intensities from panels (E) and (F). (H) Hematoxylin and eosin (H&E) staining of normal and atherosclerotic areas of the blood vessel. Scale bar = 1000 μm. Reprinted with permission from ref. 195. Copyright 2023 American Chemical Society.

for the specific imaging of fatty liver conditions in AS and OB mouse models.

AS is the leading cause of cardiovascular diseases worldwide,[204,205] characterized by the buildup of lipid-rich plaques in arteries that can lead to heart attacks and strokes.[206] Cathepsin B (CTB), an enzyme present in macrophages, is crucial in plaque formation and acts as a key biomarker for identifying vulnerable plaques and assessing cardiovascular risk.[207–210] However, the use of molecular imaging to track CTB faced challenges in probe penetration and specificity, limiting the identification of high-risk plaques. Given that atherosclerotic plaques largely consist of foam cells derived from macrophages,[211] targeting lipid levels could improve the differentiation of atherosclerotic from normal tissues.[212–214] This highlighted the need for more accurate and effective methods to measure CTB activity in plaques to better manage cardiovascular risk.

Zhang and colleagues created a CTB-responsive, lipid-sensitive probe, **L-CRP**, for precise imaging of CTB in atherosclerotic plaques.[195] **L-CRP** featured a hydrophilic CTB-responsive dipeptide, a lipophilic alkyl chain for nanoparticle formation, and a caged hemicyanine structure that prevented charge transfer until CTB cleaved the dipeptide. This cleavage triggered monomer formation in lipid-rich environments, enhancing photoacoustic (PA) and fluorescence signals (Fig. 15(A)).[195] Unlike the control probe **CRP**, **L-CRP** specifically activated in the presence of both CTB and lipids, avoiding false positives from other molecules. Its design enabled **L-CRP** to target CTB activity within foam cells rich in lipids, distinguishing them from other cell types like M1 macrophages (Fig. 15(B)–(D)). *In vivo* experiments with atherosclerosis-induced ApoE$^{-/-}$ mice showed **L-CRP** effectively highlighting atherosclerotic lesions, confirmed by various staining methods, and differentiated them from healthy tissues.[195] This specificity, demonstrated in human artery tissues (Fig. 15(E)–(H)), underscored **L-CRP**'s potential for clinical use in identifying atherosclerotic enzymatic activity, offering a new avenue for cardiovascular disease management.[195]

3.8 Plasma membranes-mediated DIE

Effective plasma membrane (PM) staining is essential for scientific studies like cell identification, translocation assays, and exploring PM dynamics, given its vital role in processes

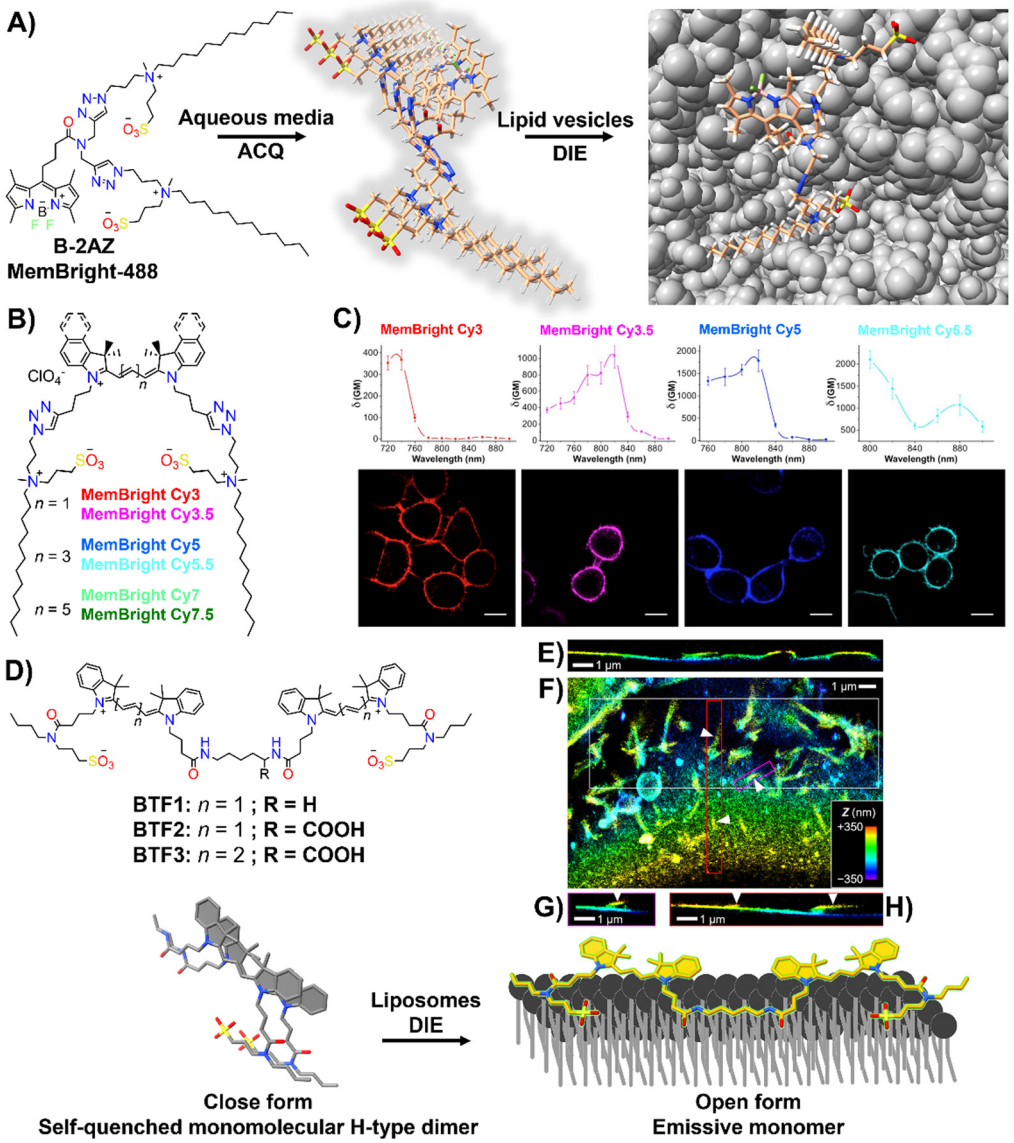

Fig. 16 (A) Chemical structure of **B-2AZ** (**MemBright-488**), illustrating its propensity for intermolecular aggregation and lipid-vesicle-induced disaggregation. (B) Chemical structures of various **MemBright** dyes. (C) Graphs of two-photon absorption cross-sections alongside images of KB cells stained with **MB-Cy3**, **MB-Cy3.5**, **MB-Cy5**, and **MB-Cy5.5**. Reprinted with permission from ref. 35. Copyright 2019 Elsevier. (D) Chemical structures of Cy3-based **BTF1** and **BTF2**, and Cy5-based **BTF3** probes, highlighting the concept of a switchable cyanine-based intramolecular dimeric probe that becomes fluorescent upon reversible binding to biomembranes. (E)–(H) 3D-PAINT with **BTF2** reveals the intricate 3D structures and dynamics of the plasma membrane in living cells. (E) Presented is a vertical cross-sectional view of the 3D-PAINT data from a COS-7 cell, showcasing varying membrane heights. (F) In-plane view of a different cell, emphasizing numerous nanoscale tubules. (G) and (H) Vertical cross-sectional views through the magenta (G) and red (H) boxes in (F), displaying tubules extending from the cell surface (indicated by arrowheads). Note: in the vertical cross-sectional views in (E), (G), and (H), the vertical dimension indicates depth into the sample. Reprinted with permission from ref. 63. Copyright 2022 American Chemical Society.

like cell division, endocytosis, and signal transduction.[215–218] The PM's boundary function enables the development of DIE-active probes that transition from non-fluorescent in cell media to fluorescent upon membrane contact.[35,63,196–198,219] This approach minimizes background noise and facilitates real-time, selective imaging of the membrane bilayer.

The Klymchenko group had developed a BODIPY-based dye, **B-2AZ**[196] also referred as **MemBright-488**,[196] along with six cyanine-based dyes under the **MeMBright** family,[35] which emitted from green to near-infrared (Fig. 16(A) and (B)). These intermolecularly self-assembled probes transition from non-emissive in phosphate buffer (PBS) to bright upon interaction with DOPC vesicles, mimicking the plasma membrane (PM).[35,196] They demonstrated high PM specificity, aligning with PM markers and highlighting intercellular nanotubes. The **MeMBright** probes also excelled in two-photon microscopy, confirming PM selectivity in live cells and *ex vivo* tissues (Fig. 16(C)).[35] **MB-Cy3.5**, tested for photostability, showed

exceptional resistance to photobleaching during extensive 3D liver imaging and enhanced neuron identification in brain sections.[35] Super-resolution imaging with **MB-Cy3.5** detailed dendritic spine morphologies and visualized "en-passant" synapses, proving the probes' potential in sophisticated imaging applications.[35]

The same group also focused on enhancing fluorescent probes for single molecule localization microscopy (SMLM) of cell membranes, addressing challenges in resolution, brightness, and photostability. They introduced intramolecularly formed fluorogenic dimers (**BTF1** and **BTF2**), composed of Cy3 dyes linked by cadaverine or lysine, and featuring membrane anchor sulfonate groups (Fig. 16(D)).[63] These dimers were designed to enhance PAINT imaging[220] by reducing plasma membrane affinity and facilitating on/off switching (Fig. 16(D)).[63] Spectroscopy had shown that these dimers self-quenched in PBS but brightened in organic solvents and with DOPC, indicating effective disassembly for membrane binding. **BTF2**, with a lower DOPC affinity due to its hydrophilic lysine linker, and the far-red Cy5-based **BTF3** variant, were tested in live cell microscopy, demonstrating superior single-molecule fluorescence switching, greater brightness, and enhanced localization precision compared to commercially available PM stains.[63] **BTF2** also allowed 3D imaging of COS-7 fibroblast-like cell membranes, unveiling dynamic membrane reshaping (Fig. 16(E)–(H)). **BTF3** further improved super-resolution imaging over monomeric Cy5-based DiD dye, highlighting diverse nanoscopic membrane structures with limited dye movement.[63] This advancement introduced dimer-based probes that significantly improved super-resolution imaging of cell membranes by reducing dye diffusion and enhancing imaging resolution and stability.

An alternative method based on DIE to stain the PM was proposed by Xu and colleagues.[198] They had developed a series of amide-containing receptors for Zn^{2+}, incorporating a naphthalimide fluorophore and a hydrophobic alkyl chain of varying lengths, designated as **ZTRS-alkyl**, to anchor to membranes.[198] Notably, the dodecyl-substituted probe, **ZTRS-C_{12}**, formed nanoaggregates in aqueous solution (Fig. 17). In the presence of Zn^{2+}, **ZTRS-C_{12}** displayed a 1.5-fold increase in fluorescence. However, when dissolved in a mixed solution of HEPES buffer and CH_3CN, serving as a disaggregating solvent, **ZTRS-C_{12}** exhibited a significant 13-fold enhancement in fluorescence, demonstrating its ability to sense Zn^{2+} in its monomeric form.[198] In the human colon cancer cell line HT-29, **ZTRS-C_{12}**, while attached to the exterior of the cell plasma membrane in a monomer-like state, initiated a fluorescence response upon complexing with Zn^{2+}. The fluorescence signal was eliminated upon the addition of EDTA, which displaces zinc from the probe complex. **ZTRS-C_{12}** demonstrated exceptional selectivity for Zn^{2+} over other biologically relevant heavy and transition metal ions.[198]

3.9 Lipid droplets- and exosomes-mediated DIE

Lipid droplets (LDs), present in organisms from prokaryotes to humans, contain a metabolic lipid core within a phospholipid monolayer membrane.[221,222] Beyond serving as lipid storage,[223] LDs are integral to processes like membrane trafficking,[224] protein degradation,[225] inflammation,[226] and are implicated in diseases

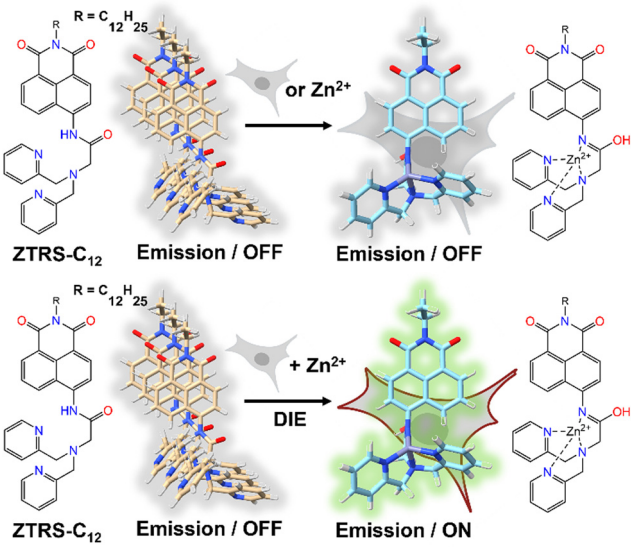

Fig. 17 Design of the fluorogenic probe **ZTRS-C_{12}** for imaging Zn^{2+} at the plasma membrane surface of living cells. In its self-assembled state, **ZTRS-C_{12}** displayed minimal fluorescence changes when introduced to cells alone or with Zn^{2+} separately (top panel). However, the simultaneous addition of **ZTRS-C_{12}** and Zn^{2+} to cells triggered its disassembly and activated the fluorescence *via* complexation with Zn^{2+} (bottom panel).

such as obesity and diabetes,[186] as well as cancer.[227] Given their varied number, size, and composition, imaging and analysing LD dynamics are essential for unravelling their biological significance.

The Klymchenko group introduced StatoMerocyanines (**SMCy**) fluorophores, based on indolenine and dioxaborine barbiturate structures connected by polymethyne chains (Fig. 18(A)).[200] These lipophilic dyes, non-emissive in water due to aggregation, exhibited up to 1700-fold fluorescence enhancement in oils (Fig. 18(B)–(D)). When incubated with KB cells, **SMCy** selectively stained LDs (Fig. 18(E) and (F)). Utilized in multicolor tissue imaging, **SMCy** dyes effectively highlighted lipid structures in mouse adipose tissue and liver, demonstrating their ability for 3D visualization and tracking of lipid-rich vesicles and LD exchange between cells, proving their suitability for advanced imaging techniques like two-photon microscopy (Fig. 18(G)).[200]

Zhou and team introduced **CM2P**, a two-photon lipophilic coumarin-based probe for super-resolution imaging and dynamic LD tracking (Fig. 19(A)).[29] Exhibiting ACQ in PBS and forming nanoparticles, **CM2P**'s fluorescence intensified in oil/water emulsions *via* a DIE process (Fig. 19(A)). It selectively stained LDs under both one- and two-photon imaging (Fig. 19(B) and (C)). Employed in STED microscopy, **CM2P** achieved higher resolution than conventional CLSM, and enabled real-time LD observation with two-photon microscopy (Fig. 19(D)).[29]

Exosomes are small vesicles (40–150 nm) released by cells, carrying proteins, mRNA, DNA, and microRNAs crucial for intercellular communication, inflammation, and tissue repair.[228–231] Serving as biomarkers, they provide a non-invasive means for disease diagnosis and management, with higher prevalence in tumor cells, influencing cancer development and progression.[230–233]

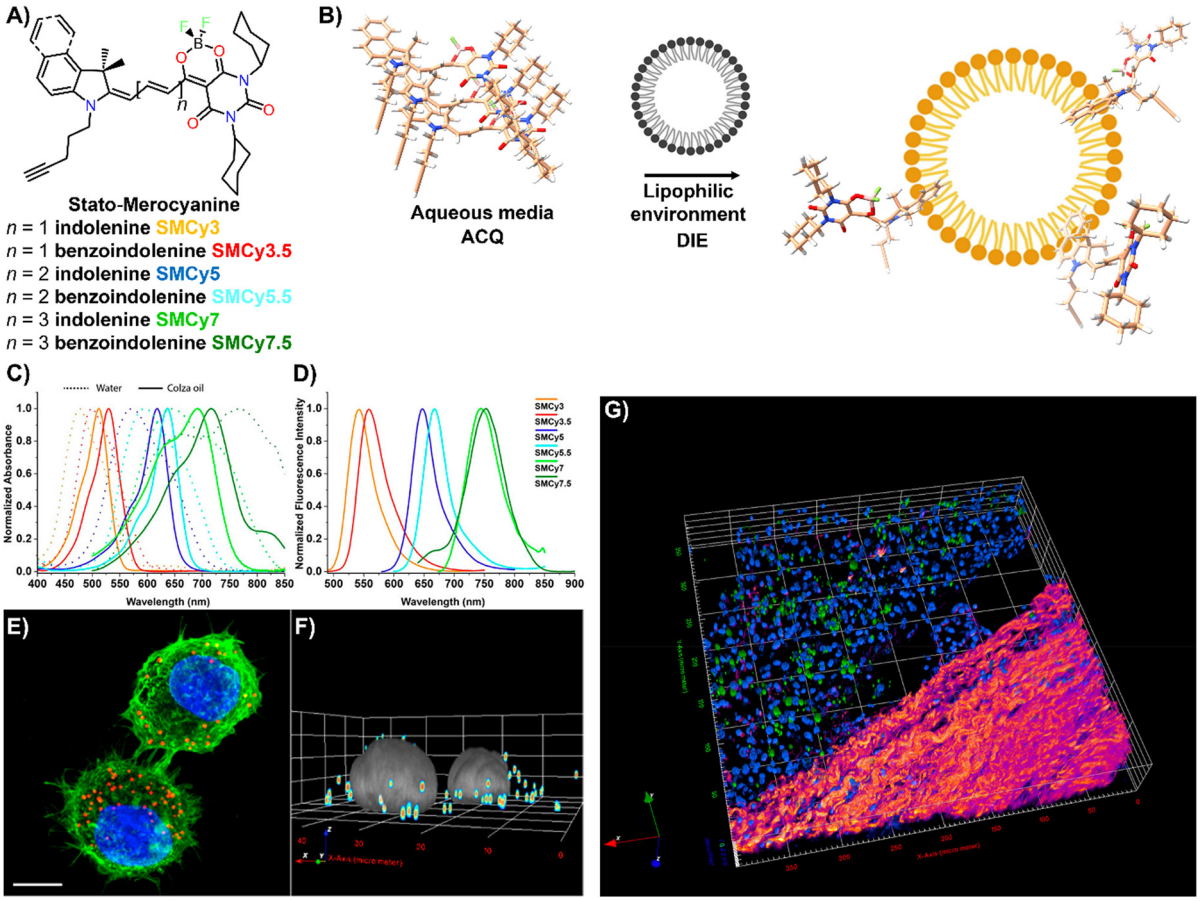

Fig. 18 (A) Chemical structures of the six **SMCy** family members. (B) Operational recognition mechanism of **SMCy** dyes. (C) and (D) Normalized absorption spectra of **SMCy** dyes in water (dashed lines) and colza oil (solid lines) (C), along with their normalized emission spectra in oil (D). (E) Maximum intensity projection image of KB cells displaying LDs with **SMCy5** (red), nuclei stained with Hoechst (blue), and plasma membranes marked by **MemBright-488** (green). Scale bar: 10 μm. (F) 3D image showing the LDs (coloured spots) and nuclei (gray). (G) Two-photon excitation 3D imaging of a mouse liver slice treated with Hoechst and **SMCy5.5**, depicting nuclei (blue), lipid droplets (green), and collagen fibers (fire-coloured). The excitation wavelength was 810 nm. Reprinted with permission from ref. 200. Copyright 2018 American Chemical Society.

Nishizawa's team developed a novel exosome detection method using an asymmetric cyanine dye, **ApoC-TRC12**, based on Thiazole Red and modified with a hydrophobic unit and a membrane-binding peptide from Apolipoprotein A-I (Fig. 20(A)).[202] In PBS, **ApoC-TRC12** forms H-type aggregates, showing broad absorption and low fluorescence, which disaggregate in DMSO. Fluorescence tests with synthetic vesicles showed that **ApoC-TRC12** lights-up with 130 nm vesicles, suggesting potential selective exosome detection through a DIE process, yet demonstrates minimal change with larger 440 nm vesicles. Tested on exosomes from K562 and A549 cells, **ApoC-TRC12** achieved rapid detection with LODs of 3.5×10^3 and 2.1×10^3 particles per μL, respectively, outperforming the commercial MemGlow 640 probe (Fig. 20(B) and (C)).[202]

4 Self-disassembly and partially unknown processes-mediated DIE

In this section, we aim to highlight how disaggregation can lead to misleading results. DIE is not solely caused by binding to specific receptors that trigger probe disassembly. Instead, DIE may also result from inherent disassembly processes or poorly understood effects (Fig. 21(A)). These inaccuracies are frequently associated with the sample preparation method, which can involve various solvents or their mixtures, the sample's duration of storage and conditions, experimental temperatures, and the presence of impurities in the sample.

In their research on sugar-binding mechanisms, Anslyn and colleagues explored the activation mechanism of a well-established boronic acid-based saccharide sensor, referred to as compound **3**, and compared its fluorescence response to that of a structurally analogous compound **4**, which lacks the boronic acid group, thereby inhibiting sugar binding (Fig. 21(B) and (C)).[234] Both compounds demonstrated fluorescence enhancements in the absence of fructose, a phenomenon attributed to an autocatalyzed disassembly process. Introducing fructose into a solution pre-equilibrated with compounds **3** and **4** resulted in a modest two-fold increase in the fluorescence intensity of compound **3**, while changes in compound **4** were minimal.[234] These results indicate that fructose may slightly boost the fluorescence of compound **3**, potentially due to a binding interaction or by promoting further disaggregation of the probe, but this does not

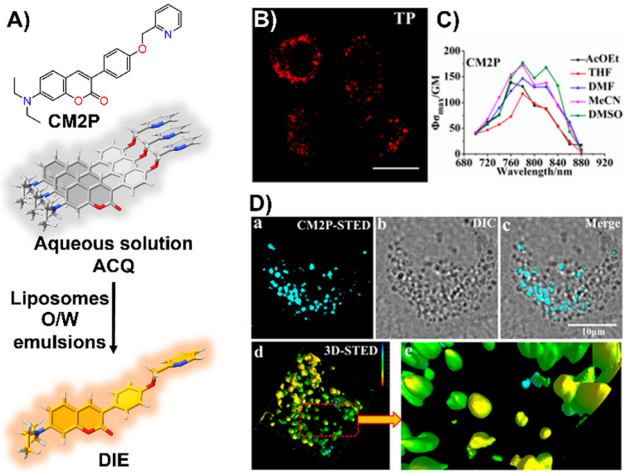

Fig. 19 (A) Chemical structure of **CM2P** and its DIE mechanism mediated by liposomes or oil/water emulsions. (B) and (C) Two-photon fluorescence imaging of HeLa cells stained with **CM2P** (B) and the two-photon molecular brightness of **CM2P** across various solvents (C). (D) Morphological characterization of LDs in live HeLa cells stained with **CM2P**: (a) STED image, (b) bright-field image, (c) merged image of (a) and (b), (d) 3D-STED image, and (e) zoomed-in view of (d). Rainbow calibration bar, *Z*-scale (0–10 μm); scale bar: 10 μm. Reprinted with permission from ref. 29. Copyright 2019 American Chemical Society.

entirely account for the sensor's activation.[234] This highlights the necessity for caution in studies that involve DIE processes with biological molecules, as autocatalyzed disaggregation may produce misleading outcomes.

Similar behaviour has been found in an entirely different sugar-binding study, in which Davis and colleagues discovered that the UV-visible absorption of tetraphenylporphine tetrasulfonate (**TPPS**), a porphyrin-based host, changed in the presence of glucose.[235] These alterations were more accurately linked to variations in the porphyrin's aggregation state rather than to direct glucose binding. The changes in **TPPS**'s UV-visible spectra upon adding glucose appeared to stem from complex, kinetically slow shifts in the porphyrin's aggregation state. Such changes could occur even without any additions to **TPPS**, and other substances like glycerol could similarly trigger these effects.[235] Titration experiments might have suggested 1 : 1 binding, but this was misleading. While these findings were specific to **TPPS**, it was probable that other simple porphyrins would exhibit similar behaviour. Consequently, claims of carbohydrate recognition by porphyrins in aqueous solutions should have been approached with caution, especially if changes in aggregation state might explain the observed phenomena.

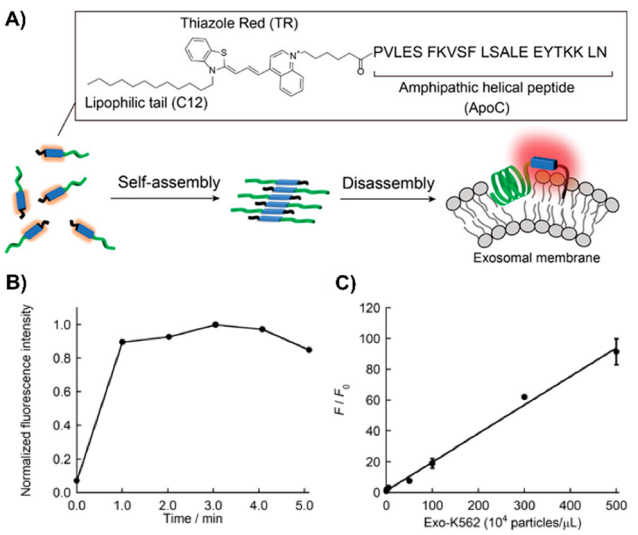

Fig. 20 (A) Schematic depiction of the self-assembly/disassembly mechanism for fluorescence sensing by **ApoC-TRC12**, used in exosome analysis. (B) Time-dependent fluorescence changes at 656 nm for **ApoC-TRC12** following the addition of exosomes derived from K562 cells (Exo-K562). (C) Calibration curve for Exo-K562 based on the fluorescence response of **ApoC-TRC12**. *F* and F_0 represent the fluorescence intensities at 656 nm with and without Exo-K562, respectively. Reprinted with permission from ref. 202. Copyright 2023 American Chemical Society.

5 Conclusions and outlook

Initially overlooked, DIE has rapidly evolved into a vibrant and expanding field of research, establishing itself as an indispensable sensing technique through significant advancements over the past decade. The shift from focusing on π–π complex packing and intermolecular interactions[32,35,124,158,196] to exploring sophisticated intramolecular dimer models[34,63,64] stabilized by covalent bonds has markedly enhanced our comprehension of the fluorescence amplification mechanisms. Discoveries such as enhanced ROS generation[102,135,158,173] and ultrasensitive fluorescence assays[29,63,81,200] have paved the way for novel applications in bioimaging, sensing, and therapeutic interventions.

Thanks to global scientific contributions, DIE research has achieved remarkable progress, addressing clinical diagnosis and pathology,[194,195] drug delivery,[126,179,180] and precision medicine.[61,95,98,108] This review emphasizes the expansion of DIE research from *in vitro* studies of biologically relevant biomacromolecules and organelles to include tissues and live animals, with DIE-active agents significantly advancing imaging techniques beyond conventional methods.

Despite the global development of numerous DIE-active materials, creating molecular aggregates with precise and consistent optical properties remains a significant challenge. Most DIE dyes exhibit H-type characteristics, leading to poorly defined molecular architectures. In contrast, J-type aggregates typically show well-defined packing behaviour, which can be controlled by incorporating specific hydrogen bonding moieties.[236] J-type structures also exhibit unique optical features, such as red-shifted absorption bands and significantly enhanced radiative decay rate (superradiance).[19] This may allow their assembly and disassembly to be finely controlled before and after binding events with biological targets, resulting in notable optical changes useful for sensing and imaging applications.

Many DIE-active molecules with superior self-assembly and molecular recognition capabilities are yet to be discovered. Interest in these molecules extends beyond their luminescent properties to their pharmacological potential and applications

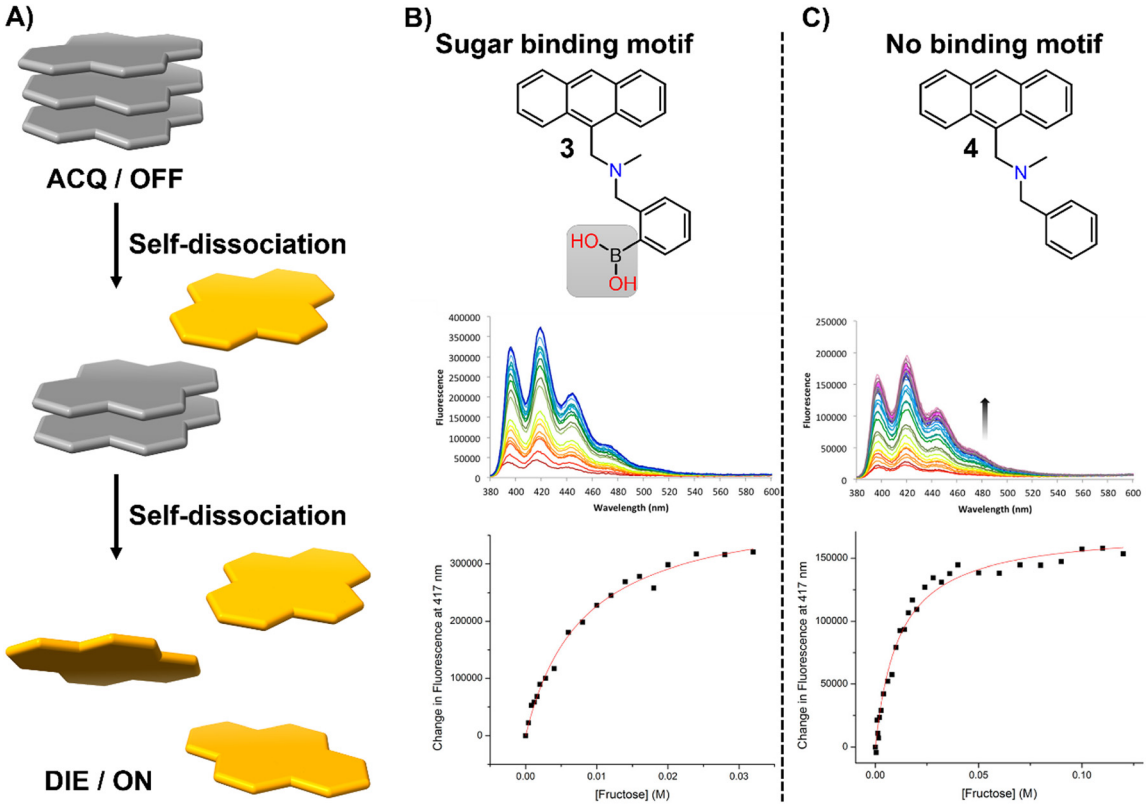

Fig. 21 (A) Schematic representation of the self-dissociative mechanism that self-assembling probes may undergo, potentially leading to artifacts and misleading results. (B) Chemical structures of compounds **3** and **4**, along with their fluorescence spectral changes associated with the presence of fructose. Reprinted with permission from ref. 234. Copyright 2017 American Chemical Society.

in diagnostics and therapy. To improve the clarity of bioimaging background signals, there is a push to develop DIE-active dyes for NIR imaging, multiphoton fluorescence microscopy, and super-resolution imaging. This development requires designing fluorescent dyes that completely quench fluorescence when aggregated and fully recover upon monomeric binding to targets, necessitating further optimization of the chemical structures of current DIE-active dyes. Artificial intelligence (AI) presents a promising avenue to revolutionize DIE research by streamlining the discovery process and cutting costs.

Numerous spectroscopic and microscopy methods, coupled with MD simulations, have been employed to decipher the disassembly mechanism of DIE-active dyes triggered by biologically relevant biomolecules. However, there remains a lack of in-depth studies focusing on elucidating the complexation processes at the atomic level using NMR spectroscopy or X-ray crystallography. Obtaining such data would have a tremendous impact on understanding the driving forces behind dye disassembly, providing unprecedented opportunities to design materials with custom-tailored recognition motifs.

Additional potential applications of DIE dyes include the development of smart materials sensitive to specific external stimuli. These dyes can be engineered to act as pH or temperature sensors, disaggregating at specific thresholds. This property is particularly useful in drug delivery systems, where DIE dyes can ensure the targeted and controlled release of drugs within specific cellular organelles in response to pH or temperature changes. Moreover, DIE dyes can be designed to respond to the presence of specific ions or heavy metals, making them valuable in medical diagnostics for monitoring electrolyte balance and in environmental monitoring for detecting pollutants.

In summary, the past decade's research into DIE-active materials has already showcased their immense potential in health and life sciences. Looking ahead, we anticipate that DIE will continue to drive groundbreaking discoveries and introduce innovative methods for understanding biological systems and enhancing therapeutic and diagnostic outcomes.

Author contributions

K. Saczuk and M. Dudek contributed to literature curation and manuscript writing, while K. Matczyszyn took part in manuscript editing. M. Deiana spearheaded the review by conceiving, designing and administering it, supervising the work, leading literature curation, manuscript writing, figure design, review and editing. All authors have read and approved the final manuscript.

Data availability

No primary research results, software or code have been included and no new data were generated or analysed as part of this review.

Conflicts of interest

There are no conflicts to declare.

Acknowledgements

M. Deiana would like to acknowledge financial support from project no. 2022/47/P/NZ5/01156, which is co-funded by the National Science Centre and the European Union's Horizon 2020 research and innovation program under the Marie Skłodowska-Curie grant agreement no. 945339. K. Matczyszyn acknowledges funding from the National Science Centre within the Opus UMO-2019/35/B/ST4/03280 project.

Notes and references

1 A. Schulz and F. Würthner, *Angew. Chem., Int. Ed.*, 2022, **61**, e202114667.
2 X. Hu, J. O. Lindner and F. Würthner, *J. Am. Chem. Soc.*, 2020, **142**, 3321–3325.
3 D. Bialas, E. Kirchner, M. I. S. Röhr and F. Würthner, *J. Am. Chem. Soc.*, 2021, **143**, 4500–4518.
4 A. P. Deshmukh, A. D. Bailey, L. S. Forte, X. Shen, N. Geue, E. M. Sletten and J. R. Caram, *J. Phys. Chem. Lett.*, 2020, **11**, 8026–8033.
5 M. Wehner and F. Würthner, *Nat. Rev. Chem.*, 2020, **4**, 38–53.
6 J. Matern, Y. Dorca, L. Sánchez and G. Fernández, *Angew. Chem., Int. Ed.*, 2019, **58**, 16730–16740.
7 A. Sorrenti, J. Leira-Iglesias, A. J. Markvoort, T. F. A. de Greef and T. M. Hermans, *Chem. Soc. Rev.*, 2017, **46**, 5476–5490.
8 J. Boekhoven, W. E. Hendriksen, G. J. M. Koper, R. Eelkema and J. H. van Esch, *Science*, 2015, **349**, 1075–1079.
9 J. Leira-Iglesias, A. Tassoni, T. Adachi, M. Stich and T. M. Hermans, *Nat. Nanotechnol.*, 2018, **13**, 1021–1027.
10 A. Mishra, S. Dhiman and S. J. George, *Angew. Chem., Int. Ed.*, 2021, **60**, 2740–2756.
11 S. Dhiman, A. Jain, M. Kumar and S. J. George, *J. Am. Chem. Soc.*, 2017, **139**, 16568–16575.
12 M. Hecht and F. Würthner, *Acc. Chem. Res.*, 2021, **54**, 642–653.
13 F. Würthner, *Acc. Chem. Res.*, 2016, **49**, 868–876.
14 K. Cai, J. Xie, D. Zhang, W. Shi, Q. Yan and D. Zhao, *J. Am. Chem. Soc.*, 2018, **140**, 5764–5773.
15 E. Feng, Y. Liu, S. Lv, D. Liu, S. Huang, Z. Li and F. Song, *Adv. Funct. Mater.*, 2022, **32**, 2209258.
16 V. Grande, B. Soberats, S. Herbst, V. Stepanenko and F. Würthner, *Chem. Sci.*, 2018, **9**, 6904–6911.
17 J. L. Banal, T. Kondo, R. Veneziano, M. Bathe and G. S. Schlau-Cohen, *J. Phys. Chem. Lett.*, 2017, **8**, 5827–5833.
18 W. P. Bricker, J. L. Banal, M. B. Stone and M. Bathe, *J. Chem. Phys.*, 2018, **149**, 024905.
19 S. Xu, H.-W. Liu, S.-Y. Huan, L. Yuan and X.-B. Zhang, *Mater. Chem. Front.*, 2021, **5**, 1076–1089.
20 J. Heo, D. P. Murale, H. Y. Yoon, V. Arun, S. Choi, E. Kim, J.-S. Lee and S. Kim, *Aggregate*, 2022, **3**, e159.
21 J. Mei, N. L. C. Leung, R. T. K. Kwok, J. W. Y. Lam and B. Z. Tang, *Chem. Rev.*, 2015, **115**, 11718–11940.
22 F. Xia, W. Fan, S. Jiang, Y. Ma, Y. Lu, J. Qi, E. Ahmad, X. Dong, W. Zhao and W. Wu, *ACS Appl. Mater. Interfaces*, 2017, **9**, 21660–21672.
23 X. Hu, W. Fan, Z. Yu, Y. Lu, J. Qi, J. Zhang, X. Dong, W. Zhao and W. Wu, *Nanoscale*, 2016, **8**, 7024–7035.
24 X. Ji, Y. Cai, X. Dong, W. Wu and W. Zhao, *Nanoscale*, 2023, **15**, 9290–9296.
25 H. He, S. Jiang, Y. Xie, Y. Lu, J. Qi, X. Dong, W. Zhao, Z. Yin and W. Wu, *Nanoscale Horiz.*, 2018, **3**, 397–407.
26 S. Atchimnaidu, D. Perumal, K. S. Harikrishanan, H. V. P. Thelu and R. Varghese, *Nanoscale*, 2020, **12**, 11858–11862.
27 F. Würthner, *Angew. Chem., Int. Ed.*, 2020, **59**, 14192–14196.
28 H. Wang, Q. Li, P. Alam, H. Bai, V. Bhalla, M. R. Bryce, M. Cao, C. Chen, S. Chen, X. Chen, Y. Chen, Z. Chen, D. Dang, D. Ding, S. Ding, Y. Duo, M. Gao, W. He, X. He, X. Hong, Y. Hong, J.-J. Hu, R. Hu, X. Huang, T. D. James, X. Jiang, G.-I. Konishi, R. T. K. Kwok, J. W. Y. Lam, C. Li, H. Li, K. Li, N. Li, W.-J. Li, Y. Li, X.-J. Liang, Y. Liang, B. Liu, G. Liu, X. Liu, X. Lou, X.-Y. Lou, L. Luo, P. R. McGonigal, Z.-W. Mao, G. Niu, T. C. Owyong, A. Pucci, J. Qian, A. Qin, Z. Qiu, A. L. Rogach, B. Situ, K. Tanaka, Y. Tang, B. Wang, D. Wang, J. Wang, W. Wang, W.-X. Wang, W.-J. Wang, X. Wang, Y.-F. Wang, S. Wu, Y. Wu, Y. Xiong, R. Xu, C. Yan, S. Yan, H.-B. Yang, L.-L. Yang, M. Yang, Y.-W. Yang, J. Yoon, S.-Q. Zang, J. Zhang, P. Zhang, T. Zhang, X. Zhang, N. Zhao, Z. Zhao, J. Zheng, L. Zheng, Z. Zheng, M.-Q. Zhu, W.-H. Zhu, H. Zou and B. Z. Tang, *ACS Nano*, 2023, **17**, 14347–14405.
29 H. Xu, H. Zhang, G. Liu, L. Kong, X. Zhu, X. Tian, Z. Zhang, R. Zhang, Z. Wu, Y. Tian and H. Zhou, *Anal. Chem.*, 2019, **91**, 977–982.
30 E. G. Kaye, K. Kailass, O. Sadovski and A. A. Beharry, *ACS Med. Chem. Lett.*, 2021, **12**, 1295–1301.
31 D. Zhai, W. Xu, L. Zhang and Y.-T. Chang, *Chem. Soc. Rev.*, 2014, **43**, 2402–2411.
32 M. Deiana, K. Chand, J. Jamroskovic, I. Obi, E. Chorell and N. Sabouri, *Angew. Chem., Int. Ed.*, 2020, **59**, 896–902.
33 V. Grande, C.-A. Shen, M. Deiana, M. Dudek, J. Olesiak-Banska, K. Matczyszyn and F. Würthner, *Chem. Sci.*, 2018, **9**, 8375–8381.
34 F. Bouhedda, K. T. Fam, M. Collot, A. Autour, S. Marzi, A. Klymchenko and M. Ryckelynck, *Nat. Chem. Biol.*, 2020, **16**, 69–76.
35 M. Collot, P. Ashokkumar, H. Anton, E. Boutant, O. Faklaris, T. Galli, Y. Mély, L. Danglot and A. S. Klymchenko, *Cell Chem. Biol.*, 2019, **26**, 600–614.
36 A. Das, S. Das, A. Biswas and N. Chattopadhyay, *J. Phys. Chem. B*, 2021, **125**, 13482–13493.
37 P. Paul, S. Samanta, A. Chatterjee, A. Mallick and T. Majumdar, *Phys. Chem. Chem. Phys.*, 2023, **25**, 10166–10174.

38 Q. Bai, S. Zhang, H. Chen, T. Sun, C. Redshaw, J.-X. Zhang, X.-L. Ni, G. Wei and Z. Tao, *ChemistrySelect*, 2017, **2**, 2569–2573.
39 M. Sayed, S. Jha and H. Pal, *Phys. Chem. Chem. Phys.*, 2017, **19**, 24166–24178.
40 Q. Wang, Q. Zhang, Q.-W. Zhang, X. Li, C.-X. Zhao, T.-Y. Xu, D.-H. Qu and H. Tian, *Nat. Commun.*, 2020, **11**, 158.
41 H. Yin, F. Dumur, Y. Niu, M. M. Ayhan, O. Grauby, W. Liu, C. Wang, D. Siri, R. Rosas, A. Tonetto, D. Gigmes, R. Wang, D. Bardelang and O. Ouari, *ACS Appl. Mater. Interfaces*, 2017, **9**, 33220–33228.
42 H.-B. Cheng, Z. Sun, N. Kwon, R. Wang, Y. Cui, C. O. Park and J. Yoon, *Chem. – Eur. J.*, 2019, **25**, 3501–3504.
43 P. Zhang, M.-S. Zhu, H. Luo, Q. Zhang, L.-E. Guo, Z. Li and Y.-B. Jiang, *Anal. Chem.*, 2017, **89**, 6210–6215.
44 L.-X. Huang, Q. Guo, Y. Chen, P. Verwilst, S. Son, J.-B. Wu, Q.-Y. Cao and J. S. Kim, *Chem. Commun.*, 2019, **55**, 14135–14138.
45 B. Muthuraj, S. R. Chowdhury, S. Mukherjee, C. R. Patra and P. K. Iyer, *RSC Adv.*, 2015, **5**, 28211–28218.
46 L. Liu, C. Liu, L. Wang, X.-C. Shen and H. Chen, *Sens. Actuators, B*, 2022, **371**, 132542.
47 Y. Hu, Y. Wang, X. Wen, Y. Pan, X. Cheng, R. An, G. Gao, H.-Y. Chen and D. Ye, *Research*, 2020, 4087069.
48 J. Yang, C.-C. Dong, X.-L. Chen, X. Sun, J.-Y. Wei, J.-F. Xiang, J. L. Sessler and H.-Y. Gong, *J. Am. Chem. Soc.*, 2019, **141**, 4597–4612.
49 L. K. Kumawat, A. A. Abogunrin, M. Kickham, J. Pardeshi, O. Fenelon, M. Schroeder and R. B. P. Elmes, *Front. Chem.*, 2019, **7**, 354.
50 B. Andreiuk, A. Reisch, E. Bernhardt and A. S. Klymchenko, *Chem. – Asian J.*, 2019, **14**, 836–846.
51 V. Kshtriya, B. Koshti, D. K. Pandey, S. Kharbanda, C. Kanth P, D. K. Singh, D. Bhatia and N. Gour, *Soft Matter*, 2021, **17**, 4304–4316.
52 M. Qiao, R. Zhang, S. Liu, J. Liu, L. Ding and Y. Fang, *ACS Appl. Mater. Interfaces*, 2022, **14**, 32706–32718.
53 J. Fan, L. Ding and Y. Fang, *Langmuir*, 2019, **35**, 326–341.
54 T. Jing and L. Yan, *Talanta*, 2017, **170**, 185–192.
55 W. Tian, J. Zhang, J. Yu, J. Wu, H. Nawaz, J. Zhang, J. He and F. Wang, *Adv. Opt. Mater.*, 2016, **4**, 2044–2050.
56 X. Liu, K. Jia, Y. Wang, W. Shao, C. Yao, L. Peng, D. Zhang, X.-Y. Hu and L. Wang, *ACS Appl. Mater. Interfaces*, 2017, **9**, 4843–4850.
57 Y. Liu, C. Xu, L. Teng, H.-W. Liu, T.-B. Ren, S. Xu, X. Lou, H. Guo, L. Yuan and X.-B. Zhang, *Chem. Commun.*, 2020, **56**, 1956–1959.
58 K. Sou, L. Y. Chan, S. Arai and C.-L. K. Lee, *Sci. Rep.*, 2019, **9**, 17991.
59 V. G. Panse, P. Vogel, W. E. Trommer and R. Varadarajan, *J. Biol. Chem.*, 2000, **275**, 18698–18703.
60 V. Grande, F. Doria, M. Freccero and F. Würthner, *Angew. Chem., Int. Ed.*, 2017, **56**, 7520–7524.
61 M. Deiana, K. Chand, J. Jamroskovic, R. N. Das, I. Obi, E. Chorell and N. Sabouri, *Nanoscale*, 2020, **12**, 12950–12957.
62 M. Deiana, K. Chand, E. Chorell and N. Sabouri, *J. Phys. Chem. Lett.*, 2023, **14**, 1862–1869.
63 I. O. Aparin, R. Yan, R. Pelletier, A. A. Choi, D. I. Danylchuk, K. Xu and A. S. Klymchenko, *J. Am. Chem. Soc.*, 2022, **144**, 18043–18053.
64 L. Esteoulle, F. Daubeuf, M. Collot, S. Riché, T. Durroux, D. Brasse, P. Marchand, J. Karpenko, A. S. Klymchenko and D. Bonnet, *Chem. Sci.*, 2020, **11**, 6824–6829.
65 V. M. Farzan, M. V. Kvach, I. O. Aparin, D. E. Kireev, T. A. Prikazchikova, A. V. Ustinov, V. V. Shmanai, G. A. Shipulin, V. A. Korshun and T. S. Zatsepin, *Talanta*, 2019, **194**, 226–232.
66 L. F. Kessler, A. Balakrishnan, N. S. Deußner-Helfmann, Y. Li, M. Mantel, M. Glogger, H.-D. Barth, M. S. Dietz and M. Heilemann, *Angew. Chem., Int. Ed.*, 2023, **62**, e202307538.
67 A. M. D'Amico and K. M. Vasquez, *DNA Repair*, 2021, **99**, 103049.
68 F. J. Groelly, M. Fawkes, R. A. Dagg, A. N. Blackford and M. Tarsounas, *Nat. Rev. Cancer*, 2023, **23**, 78–94.
69 T. Sakamoto, D. Hasegawa and K. Fujimoto, *Org. Biomol. Chem.*, 2018, **16**, 7157–7162.
70 M. Deiana, B. Mettra, K. Matczyszyn, D. Pitrat, J. Olesiak-Banska, C. Monnereau, C. Andraud and M. Samoc, *Biomacromolecules*, 2016, **17**, 3609–3618.
71 H. Blom and J. Widengren, *Chem. Rev.*, 2017, **117**, 7377–7427.
72 K. D. Makova and M. H. Weissensteiner, *Trends Genet.*, 2023, **39**, 109–124.
73 D. Varshney, J. Spiegel, K. Zyner, D. Tannahill and S. Balasubramanian, *Nat. Rev. Mol. Cell Biol.*, 2020, **21**, 459–474.
74 N. Kosiol, S. Juranek, P. Brossart, A. Heine and K. Paeschke, *Mol. Cancer*, 2021, **20**, 40.
75 G. Biffi, D. Tannahill, J. McCafferty and S. Balasubramanian, *Nat. Chem.*, 2013, **5**, 182–186.
76 R. Hänsel-Hertsch, D. Beraldi, S. V. Lensing, G. Marsico, K. Zyner, A. Parry, M. Di Antonio, J. Pike, H. Kimura, M. Narita, D. Tannahill and S. Balasubramanian, *Nat. Genet.*, 2016, **48**, 1267–1272.
77 R. Hänsel-Hertsch, A. Simeone, A. Shea, W. W. I. Hui, K. G. Zyner, G. Marsico, O. M. Rueda, A. Bruna, A. Martin, X. Zhang, S. Adhikari, D. Tannahill, C. Caldas and S. Balasubramanian, *Nat. Genet.*, 2020, **52**, 878–883.
78 M. Deiana, J. Jamroskovic, I. Obi and N. Sabouri, *Chem. Commun.*, 2020, **56**, 14251–14254.
79 M. Deiana, M. Mosser, T. Le Bahers, E. Dumont, M. Dudek, S. Denis-Quanquin, N. Sabouri, C. Andraud, K. Matczyszyn, C. Monnereau and L. Guy, *Nanoscale*, 2021, **13**, 13795–13808.
80 S. Neidle, *Nat. Rev. Chem.*, 2017, **1**, 0041.
81 S. Liu, L. Bu, Y. Zhang, J. Yan, L. Li, G. Li, Z. Song and J. Huang, *Anal. Chem.*, 2021, **93**, 5267–5276.
82 M. Deiana, I. Obi, M. Andreasson, S. Tamilselvi, K. Chand, E. Chorell and N. Sabouri, *ACS Chem. Biol.*, 2021, **16**, 1365–1376.
83 M. Zuffo, A. Guédin, E.-D. Leriche, F. Doria, V. Pirota, V. Gabelica, J.-L. Mergny and M. Freccero, *Nucleic Acids Res.*, 2018, **46**, e115–e115.

84 F. Doria, M. Nadai, M. Zuffo, R. Perrone, M. Freccero and S. N. Richter, *Chem. Commun.*, 2017, **53**, 2268–2271.
85 M. Zuffo, F. Doria, S. Botti, G. Bergamaschi and M. Freccero, *Biochim. Biophys. Acta, Gen. Subj.*, 2017, **1861**, 1303–1311.
86 H. Yao, S. Liu, Z. Xing, Y. Miao, Z. Song, G. Li and J. Huang, *Anal. Chem.*, 2022, **94**, 15231–15239.
87 Y. Dong and M.-H. Hu, *Bioorg. Chem.*, 2023, **141**, 106879.
88 H.-Z. He, K. Li, K.-K. Yu, P.-L. Lu, M.-L. Feng, S.-Y. Chen and X.-Q. Yu, *Chem. Commun.*, 2020, **56**, 6870–6873.
89 X.-D. Wang, Y.-S. Liu and M.-H. Hu, *Bioorg. Chem.*, 2024, **143**, 107006.
90 L.-X. Wang, J.-T. Zhang, X. Sun, D.-W. Yang and Y.-L. Tang, *Dyes Pigm.*, 2021, **185**, 108882.
91 L. Guan, Y. Zhou, X. Li, Y. Mao, A. Li, Y. Fu, W. Liu, S. Dong, Z. Liang, Y. Zhang, Q. Zhao and L. Zhang, *Anal. Chem.*, 2023, **95**, 9288–9296.
92 G.-F. Liu, Y.-S. Chen, Z.-L. Wang, D. Gu and M.-Q. Wang, *Dyes Pigm.*, 2024, **225**, 112107.
93 H.-Y. Li, H.-W. Cao, X.-X. Lang, Y.-S. Chen and M.-Q. Wang, *J. Mater. Chem. B*, 2022, **10**, 7772–7779.
94 M.-Q. Wang, J.-J. Gao, Q.-Q. Yu and H.-B. Liu, *New J. Chem.*, 2020, **44**, 13557–13564.
95 J. Jamroskovic, M. Doimo, K. Chand, I. Obi, R. Kumar, K. Brännström, M. Hedenström, R. Nath Das, A. Akhunzianov, M. Deiana, K. Kasho, S. Sulis Sato, P. L. Pourbozorgi, J. E. Mason, P. Medini, D. Öhlund, S. Wanrooij, E. Chorell and N. Sabouri, *J. Am. Chem. Soc.*, 2020, **142**, 2876–2888.
96 X.-D. Wang and M.-H. Hu, *Sens. Actuators, B*, 2023, **392**, 134075.
97 M.-H. Hu, *Sens. Actuators, B*, 2021, **328**, 128990.
98 A. Pandith, Y. Luo, Y. Jang, J. Bae and Y. Kim, *Angew. Chem., Int. Ed.*, 2023, **62**, e202215049.
99 A. Pandith, U. Nagarajachari, R. K. G. Siddappa, S. Lee, C. J. Park, K. Sannathammegowda and Y. J. Seo, *Bioorg. Med. Chem.*, 2021, **35**, 116077.
100 L.-M. Zhang, Y.-X. Cui, L.-N. Zhu, J.-Q. Chu and D.-M. Kong, *Nucleic Acids Res.*, 2019, **47**, 2727–2738.
101 D. Görl and F. Würthner, *Angew. Chem., Int. Ed.*, 2016, **55**, 12094–12098.
102 M. Deiana, P. Josse, C. Dalinot, A. Osmolovskyi, P. S. Marqués, J. M. A. Castán, L. Abad Galán, M. Allain, L. Khrouz, O. Maury, T. Le Bahers, P. Blanchard, S. Dabos-Seignon, C. Monnereau, N. Sabouri and C. Cabanetos, *Commun. Chem.*, 2022, **5**, 142.
103 Y.-L. Lee, Y.-T. Chou, B.-K. Su, C.-C. Wu, C.-H. Wang, K.-H. Chang, J.-A. A. Ho and P.-T. Chou, *J. Am. Chem. Soc.*, 2022, **144**, 17249–17260.
104 V.-N. Nguyen, S. Qi, S. Kim, N. Kwon, G. Kim, Y. Yim, S. Park and J. Yoon, *J. Am. Chem. Soc.*, 2019, **141**, 16243–16248.
105 Y. Chen, S. Wang and F. Zhang, *Nat. Rev. Bioeng.*, 2023, **1**, 60–78.
106 Z. Qin, T.-B. Ren, H. Zhou, X. Zhang, L. He, Z. Li, X.-B. Zhang and L. Yuan, *Angew. Chem., Int. Ed.*, 2022, **61**, e202201541.
107 C. Li, G. Chen, Y. Zhang, F. Wu and Q. Wang, *J. Am. Chem. Soc.*, 2020, **142**, 14789–14804.
108 R.-X. Wang, Y. Ou, Y. Chen, T.-B. Ren, L. Yuan and X.-B. Zhang, *J. Am. Chem. Soc.*, 2024, **146**, 11669–11678.
109 L. Rong, J. Cao, Y. Dai, W. Chen and N. Fu, *Dyes Pigm.*, 2024, **227**, 112159.
110 B.-L. Wang and C. Jiang, *Anal. Chem.*, 2019, **91**, 1541–1547.
111 P. Le, N. Ahmed and G. W. Yeo, *Nat. Cell Biol.*, 2022, **24**, 815–824.
112 E. Tutucci, M. Vera, J. Biswas, J. Garcia, R. Parker and R. H. Singer, *Nat. Methods*, 2018, **15**, 81–89.
113 A. R. Buxbaum, G. Haimovich and R. H. Singer, *Nat. Rev. Mol. Cell Biol.*, 2015, **16**, 95–109.
114 F. Bouhedda, A. Autour and M. Ryckelynck, *Int. J. Mol. Sci.*, 2018, **19**, 44.
115 C. Li, A. G. Tebo and A. Gautier, *Int. J. Mol. Sci.*, 2017, **18**, 1473.
116 J. R. Babendure, S. R. Adams and R. Y. Tsien, *J. Am. Chem. Soc.*, 2003, **125**, 14716–14717.
117 J. S. Paige, K. Y. Wu and S. R. Jaffrey, *Science*, 2011, **333**, 642–646.
118 R. L. Strack, M. D. Disney and S. R. Jaffrey, *Nat. Methods*, 2013, **10**, 1219–1224.
119 W. Song, R. L. Strack, N. Svensen and S. R. Jaffrey, *J. Am. Chem. Soc.*, 2014, **136**, 1198–1201.
120 A. D. Ellington and J. W. Szostak, *Nature*, 1990, **346**, 818–822.
121 C. Tuerk and L. Gold, *Science*, 1990, **249**, 505–510.
122 K. Y. Han, B. J. Leslie, J. Fei, J. Zhang and T. Ha, *J. Am. Chem. Soc.*, 2013, **135**, 19033–19038.
123 K. T. Fam, R. Pelletier, F. Bouhedda, M. Ryckelynck, M. Collot and A. S. Klymchenko, *Anal. Chem.*, 2022, **94**, 6657–6664.
124 C. Yan, L. Miao, Y. Zhang, X. Zhou, G. Wang, Y. Li, Q. Qiao and Z. Xu, *Sens. Actuators, B*, 2023, **386**, 133731.
125 Y. Li, T. Ma, H. Jiang, W. Li, D. Tian, J. Zhu and Z. A. Li, *Angew. Chem., Int. Ed.*, 2022, **61**, e202203093.
126 X. Li, S. Yu, D. Lee, G. Kim, B. Lee, Y. Cho, B.-Y. Zheng, M.-R. Ke, J.-D. Huang, K. T. Nam, X. Chen and J. Yoon, *ACS Nano*, 2018, **12**, 681–688.
127 A. M. Fleming and C. J. Burrows, *J. Am. Chem. Soc.*, 2020, **142**, 1115–1136.
128 Y. Ding, A. M. Fleming and C. J. Burrows, *J. Am. Chem. Soc.*, 2017, **139**, 2569–2572.
129 A. M. Fleming, B. L. Guerra Castañaza Jenkins, B. A. Buck and C. J. Burrows, *J. Am. Chem. Soc.*, 2024, **146**, 11364–11370.
130 W. Chen, Y. Zhang, H.-B. Yi, F. Wang, X. Chu and J.-H. Jiang, *Angew. Chem., Int. Ed.*, 2023, **62**, e202300162.
131 M. Deiana, J. M. Andrés Castán, P. Josse, A. Kahsay, D. P. Sánchez, K. Morice, N. Gillet, R. Ravindranath, A. K. Patel, P. Sengupta, I. Obi, E. Rodriguez-Marquez, L. Khrouz, E. Dumont, L. Abad Galán, M. Allain, B. Walker, H. S. Ahn, O. Maury, P. Blanchard, T. Le Bahers, D. Öhlund, J. von Hofsten, C. Monnereau, C. Cabanetos and N. Sabouri, *Nucleic Acids Res.*, 2023, **51**, 6264–6285.

132 M. Cheng, Y.-X. Cui, J. Wang, J. Zhang, L.-N. Zhu and D.-M. Kong, *ACS Appl. Mater. Interfaces*, 2019, **11**, 13158–13167.
133 A. Ferino, G. Nicoletto, F. D'Este, S. Zorzet, S. Lago, S. N. Richter, A. Tikhomirov, A. Shchekotikhin and L. E. Xodo, *J. Med. Chem.*, 2020, **63**, 1245–1260.
134 Q.-y Ma, X. Li, W. Zhou, X.-f Li, Y.-c Liu, G.-l Feng, H. Tan, Y. Zhang and G.-w Xing, *Chem. Commun.*, 2023, **59**, 10287–10290.
135 Z. Hu, D. Wang, Q. Zhou, J. Jie and H. Su, *J. Phys. Chem. B*, 2024, **128**, 576–584.
136 C. Okamoto, A. Momotake and Y. Yamamoto, *J. Phys. Chem. B*, 2023, **127**, 4514–4522.
137 Y. Wang, F. Huo and C. Yin, *J. Phys. Chem. B*, 2024, **128**, 1121–1138.
138 Z.-G. Wang, X.-J. Yan, H.-B. Liu, D.-L. Zhang, W. Liu, C.-Z. Xie, Q.-Z. Li and J.-Y. Xu, *J. Mater. Chem. B*, 2020, **8**, 8346–8355.
139 M. Sasmal, A. S. Musha Islam, D. Moni, D. Maiti, A. Dutta and M. Ali, *ACS Appl. Bio Mater.*, 2022, **5**, 5854–5864.
140 Z. Zheng, H. Li, S. Sun and Y. Xu, *ACS Appl. Mater. Interfaces*, 2018, **10**, 44336–44343.
141 E. N. Hoogenboezem and C. L. Duvall, *Adv. Drug Delivery Rev.*, 2018, **130**, 73–89.
142 P. Anees, S. Sreejith and A. Ajayaghosh, *J. Am. Chem. Soc.*, 2014, **136**, 13233–13239.
143 Y.-R. Wang, L. Feng, L. Xu, Y. Li, D.-D. Wang, J. Hou, K. Zhou, Q. Jin, G.-B. Ge, J.-N. Cui and L. Yang, *Chem. Commun.*, 2016, **52**, 6064–6067.
144 J. Qu, W. Meador, P. Cheah, E. E. L. Tanner, J. Delcamp and Y. Zhao, *RSC Adv.*, 2023, **13**, 27549–27557.
145 J.-Z. Li, H.-L. Lin, H.-Y. Li, H.-W. Cao, X.-X. Lang, Y.-S. Chen, H.-W. Chen and M.-Q. Wang, *Dyes Pigm.*, 2023, **216**, 111357.
146 G. B. Guseva, A. A. Ksenofontov, P. S. Bocharov, E. V. Antina and L. E. Nikitina, *J. Mol. Liq.*, 2023, **371**, 121078.
147 L. P. Jameson, N. W. Smith, O. Annunziata and S. V. Dzyuba, *Phys. Chem. Chem. Phys.*, 2016, **18**, 14182–14185.
148 N. Shivran, M. Koli, G. Chakraborty, A. P. Srivastava, S. Chattopadhyay and S. Mula, *Org. Biomol. Chem.*, 2021, **19**, 7920–7929.
149 C. Yu, W. Miao, J. Wang, E. Hao and L. Jiao, *ACS Omega*, 2017, **2**, 3551–3561.
150 C. Li, T. Wang, M. Fan, N. Wang, X. Lin, Y. Sun and X. Cui, *Nano Lett.*, 2022, **22**, 1954–1962.
151 Z. Luo, T. Lv, K. Zhu, Y. Li, L. Wang, J. J. Gooding, G. Liu and B. Liu, *Angew. Chem., Int. Ed.*, 2020, **59**, 3131–3136.
152 L. Long, X. Tan, Z. Liu, Y. Liu, X. Cao and C. Shi, *Photochem. Photobiol.*, 2022, **98**, 935–944.
153 S. Samanta, S. Halder and G. Das, *Anal. Chem.*, 2018, **90**, 7561–7568.
154 X. Fan, Q. He, S. Sun, H. Li, Y. Pei and Y. Xu, *Chem. Commun.*, 2016, **52**, 1178–1181.
155 J. Park and Y. Kim, *ChemBioChem*, 2019, **20**, 350–354.
156 T. Gao, S. Yang, X. Cao, J. Dong, N. Zhao, P. Ge, W. Zeng and Z. Cheng, *Anal. Chem.*, 2017, **89**, 10085–10093.
157 Y. Yu, Y. Huang, F. Hu, Y. Jin, G. Zhang, D. Zhang and R. Zhao, *Anal. Chem.*, 2016, **88**, 6374–6381.
158 X. Li, S. Yu, Y. Lee, T. Guo, N. Kwon, D. Lee, S. C. Yeom, Y. Cho, G. Kim, J.-D. Huang, S. Choi, K. T. Nam and J. Yoon, *J. Am. Chem. Soc.*, 2019, **141**, 1366–1372.
159 F. Wong, *Nat. Clin. Pract. Gastroenterol. Hepatol.*, 2007, **4**, 43–51.
160 A. N. Friedman and S. Z. Fadem, *J. Am. Soc. Nephrol.*, 2010, **21**, 223–230.
161 K. Mizusawa, Y. Takaoka and I. Hamachi, *J. Am. Chem. Soc.*, 2012, **134**, 13386–13395.
162 I. A. Karpenko, M. Collot, L. Richert, C. Valencia, P. Villa, Y. Mély, M. Hibert, D. Bonnet and A. S. Klymchenko, *J. Am. Chem. Soc.*, 2015, **137**, 405–412.
163 K. T. Fam, L. Saladin, A. S. Klymchenko and M. Collot, *Chem. Commun.*, 2021, **57**, 4807–4810.
164 K. T. Fam, M. Collot and A. S. Klymchenko, *Chem. Sci.*, 2020, **11**, 8240–8248.
165 G. T. Ducharme, Z. LaCasse, T. Sheth, I. V. Nesterova and E. E. Nesterov, *Angew. Chem., Int. Ed.*, 2020, **59**, 8440–8444.
166 K. Mizusawa, Y. Ishida, Y. Takaoka, M. Miyagawa, S. Tsukiji and I. Hamachi, *J. Am. Chem. Soc.*, 2010, **132**, 7291–7293.
167 M. Mohamed, A. K. Klenke, M. V. Anokhin, H. Amadou, P. J. Bothwell, B. Conroy, E. E. Nesterov and I. V. Nesterova, *ACS Sens.*, 2023, **8**, 1109–1118.
168 T. Yoshii, K. Mizusawa, Y. Takaoka and I. Hamachi, *J. Am. Chem. Soc.*, 2014, **136**, 16635–16642.
169 T.-C. Hou, Y.-Y. Wu, P.-Y. Chiang and K.-T. Tan, *Chem. Sci.*, 2015, **6**, 4643–4649.
170 P. Ashokkumar, M. Collot and A. S. Klymchenko, *Chem. – Eur. J.*, 2021, **27**, 6795–6803.
171 W. Wang, Y. Zhang, H. Zhao, X. Zhuang, H. Wang, K. He, W. Xu, Y. Kang, S. Chen, S. Zeng and L. Qian, *Chem. Sci.*, 2021, **12**, 13477–13482.
172 T. C. Pham, V.-N. Nguyen, Y. Choi, S. Lee and J. Yoon, *Chem. Rev.*, 2021, **121**, 13454–13619.
173 X. Li, C. y Kim, S. Lee, D. Lee, H.-M. Chung, G. Kim, S.-H. Heo, C. Kim, K.-S. Hong and J. Yoon, *J. Am. Chem. Soc.*, 2017, **139**, 10880–10886.
174 C. S. Jin, L. Cui, F. Wang, J. Chen and G. Zheng, *Adv. Healthcare Mater.*, 2014, **3**, 1240–1249.
175 D. Li, X.-Z. Wang, L.-F. Yang, S.-C. Li, Q.-Y. Hu, X. Li, B.-Y. Zheng, M.-R. Ke and J.-D. Huang, *ACS Appl. Mater. Interfaces*, 2019, **11**, 36435–36443.
176 X. Li, J. S. Oh, Y. Lee, E. C. Lee, M. Yang, N. Kwon, T. W. Ha, D.-Y. Hong, Y. Song, H. K. Kim, B. H. Song, S. Choi, M. R. Lee and J. Yoon, *Biomater. Res.*, 2023, **27**, 23.
177 H. Liu, L.-L. Lv, H. Wen, D.-M. Zhao, J. Wu, M.-R. Ke, B.-Y. Zheng, J. Li, X. Li and J.-D. Huang, *ACS Appl. Mater. Interfaces*, 2022, **14**, 28581–28590.
178 B. Cao, M. Yang, Y. Zhu, X. Qu and C. Mao, *Adv. Mater.*, 2014, **26**, 4627–4631.
179 X. Li, C. y Kim, J. M. Shin, D. Lee, G. Kim, H.-M. Chung, K.-S. Hong and J. Yoon, *Biomaterials*, 2018, **187**, 18–26.
180 X. Li, H. Fan, T. Guo, H. Bai, N. Kwon, K. H. Kim, S. Yu, Y. Cho, H. Kim, K. T. Nam, J. Yoon, X.-B. Zhang and W. Tan, *ACS Nano*, 2019, **13**, 6702–6710.

181 E. Fahy, S. Subramaniam, R. C. Murphy, M. Nishijima, C. R. H. Raetz, T. Shimizu, F. Spener, G. van Meer, M. J. O. Wakelam and E. A. Dennis, *J. Lipid Res.*, 2009, **50**, S9–S14.
182 S. Neugebauer, E. J. Giamarellos-Bourboulis, A. Pelekanou, A. Marioli, F. Baziaka, I. Tsangaris, M. Bauer and M. Kiehntopf, *Crit. Care Med.*, 2016, **44**, 1649–1662.
183 L. S. Eberlin, I. Norton, A. L. Dill, A. J. Golby, K. L. Ligon, S. Santagata, R. G. Cooks and N. Y. R. Agar, *Cancer Res.*, 2012, **72**, 645–654.
184 B. D. Levy, C. B. Clish, B. Schmidt, K. Gronert and C. N. Serhan, *Nat. Immunol.*, 2001, **2**, 612–619.
185 E. J. Delikatny, S. Chawla, D.-J. Leung and H. Poptani, *NMR Biomed.*, 2011, **24**, 592–611.
186 N. Krahmer, R. V. Farese and T. C. Walther, *EMBO Mol. Med.*, 2013, **5**, 973–983.
187 F. Baenke, B. Peck, H. Miess and A. Schulze, *Dis. Models & Mech.*, 2013, **6**, 1353–1363.
188 P. C. Calder, *J. Parenter. Enteral Nutr.*, 2015, **39**, 18S–32S.
189 M. L. Kraft, *Front. Cell Dev. Biol.*, 2017, **4**, 154.
190 D. Hishikawa, T. Hashidate, T. Shimizu and H. Shindou, *J. Lipid Res.*, 2014, **55**, 799–807.
191 M. H. Faulds, C. Zhao, K. Dahlman-Wright and J.-Å. Gustafsson, *J. Endocrinol.*, 2012, **212**, 3–12.
192 E. Adriaenssens, S. Lottin, T. Dugimont, W. Fauquette, J. Coll, J. P. Dupouy, B. Boilly and J. J. Curgy, *Oncogene*, 1999, **18**, 4460–4473.
193 J. Krämer, R. Kang, L. M. Grimm, L. De Cola, P. Picchetti and F. Biedermann, *Chem. Rev.*, 2022, **122**, 3459–3636.
194 K. Wang, X.-L. Wen, X.-Y. Chen, Y. Yue, Y.-S. Yang, H.-L. Zhu, M.-Y. Wang and H.-X. Jiang, *Anal. Chem.*, 2024, **96**, 2264–2272.
195 Y. Ma, J. Shang, L. Liu, M. Li, X. Xu, H. Cao, L. Xu, W. Sun, G. Song and X.-B. Zhang, *J. Am. Chem. Soc.*, 2023, **145**, 17881–17891.
196 M. Collot, E. Boutant, M. Lehmann and A. S. Klymchenko, *Bioconjugate Chem.*, 2019, **30**, 192–199.
197 D. Wu, S. Cheung, G. Sampedro, Z.-L. Chen, R. A. Cahill and D. F. O'Shea, *Biochim. Biophys. Acta, Biomembr.*, 2018, **1860**, 2272–2280.
198 F. Deng, L. Liu, Q. Qiao, C. Huang, L. Miao and Z. Xu, *Chem. Commun.*, 2019, **55**, 15045–15048.
199 N. Curtin, D. Wu, R. Cahill, A. Sarkar, P. M. Aonghusa, S. Zhuk, M. Barberio, M. Al-Taher, J. Marescaux, M. Diana and D. F. O'Shea, *Int. J. Med. Sci.*, 2021, **18**, 1541–1553.
200 M. Collot, T. K. Fam, P. Ashokkumar, O. Faklaris, T. Galli, L. Danglot and A. S. Klymchenko, *J. Am. Chem. Soc.*, 2018, **140**, 5401–5411.
201 N. Curtin, M. Garre, J.-B. Bodin, N. Solem, R. Méallet-Renault and D. F. O'Shea, *RSC Adv.*, 2022, **12**, 35655–35665.
202 K. Ohira, Y. Sato and S. Nishizawa, *ACS Sens.*, 2023, **8**, 522–526.
203 L. A. Díaz, J. P. Arab, A. Louvet, R. Bataller and M. Arrese, *Nat. Rev. Gastroenterol. Hepatol.*, 2023, **20**, 764–783.
204 V. Mehta and E. Tzima, *Nature*, 2016, **540**, 531–532.
205 H. Zheng, H. Li, Y. Wang, Z. Li, B. Hu, X. Li, L. Fu, H. Hu, Z. Nie, B. Zhao, D. Wei, B. W. Karlson, M. L. Bots, X. Meng, Y. Chen, Y. Wang, S. Cao, Y. Cai, D. Peng, Y. Fu, Z. Yuan, Y. Dong, G. Ma, W. Hong, E. Xu, H. Li, W. Yue, Y. Wang, Z. Zheng, N. Zhang, X. Zhang and W. Fu, *Stroke*, 2022, **53**, 3004–3013.
206 J. L. M. Björkegren and A. J. Lusis, *Cell*, 2022, **185**, 1630–1645.
207 T. Weiss-Sadan, I. Gotsman and G. Blum, *FEBS J.*, 2017, **284**, 1455–1472.
208 K. J. Moore, S. Koplev, E. A. Fisher, I. Tabas, J. L. M. Björkegren, A. C. Doran and J. C. Kovacic, *J. Am. Coll. Cardiol.*, 2018, **72**, 2181–2197.
209 E. R. H. Walter, S. M. Cooper, J. J. Boyle and N. J. Long, *Dalton Trans.*, 2021, **50**, 14486–14497.
210 I. Abd-Elrahman, K. Meir, H. Kosuge, Y. Ben-Nun, T. Weiss Sadan, C. Rubinstein, Y. Samet, M. V. McConnell and G. Blum, *Stroke*, 2016, **47**, 1101–1108.
211 B. Ma, Y. Xiao, Q. Lv, G. Li, Y. Wang and G. Fu, *Adv. Mater.*, 2023, **35**, 2206129.
212 M. Sang, Y. Huang, L. Wang, L. Chen, Nawsherwan, G. Li, Y. Wang, X. Yu, C. Dai and J. Zheng, *Adv. Sci.*, 2023, **10**, 2207066.
213 Z. Ye, M. Ji, K. Wu, J. Yang, A.-A. Liu, W. Sun, D. Ding and D. Liu, *Angew. Chem., Int. Ed.*, 2022, **61**, e202204518.
214 M. Sang, Y. Huang, Z. Liu, G. Li, Y. Wang, Z. Yuan, C. Dai and J. Zheng, *ACS Sens.*, 2023, **8**, 893–903.
215 D. Lingwood and K. Simons, *Science*, 2010, **327**, 46–50.
216 E. Sezgin, I. Levental, S. Mayor and C. Eggeling, *Nat. Rev. Mol. Cell Biol.*, 2017, **18**, 361–374.
217 S. Rello, J. C. Stockert, V. Moreno, A. Gámez, M. Pacheco, A. Juarranz, M. Cañete and A. Villanueva, *Apoptosis*, 2005, **10**, 201–208.
218 V. V. Shynkar, A. S. Klymchenko, C. Kunzelmann, G. Duportail, C. D. Muller, A. P. Demchenko, J.-M. Freyssinet and Y. Mely, *J. Am. Chem. Soc.*, 2007, **129**, 2187–2193.
219 M. Collot, R. Kreder, A. L. Tatarets, L. D. Patsenker, Y. Mely and A. S. Klymchenko, *Chem. Commun.*, 2015, **51**, 17136–17139.
220 A. Sharonov and R. M. Hochstrasser, *Proc. Natl. Acad. Sci. U. S. A.*, 2006, **103**, 18911–18916.
221 R. V. Farese and T. C. Walther, *Cell*, 2009, **139**, 855–860.
222 S. Martin and R. G. Parton, *Nat. Rev. Mol. Cell Biol.*, 2006, **7**, 373–378.
223 A. R. Thiam, R. V. Farese Jr and T. C. Walther, *Nat. Rev. Mol. Cell Biol.*, 2013, **14**, 775–786.
224 J. K. Zehmer, Y. Huang, G. Peng, J. Pu, R. G. W. Anderson and P. Liu, *Proteomics*, 2009, **9**, 914–921.
225 J. A. Olzmann, C. M. Richter and R. R. Kopito, *Proc. Natl. Acad. Sci. U. S. A.*, 2013, **110**, 1345–1350.
226 P. T. Bozza and J. P. B. Viola, *Prostaglandins, Leukotrienes Essent. Fatty Acids*, 2010, **82**, 243–250.
227 Q. Liu, Q. Luo, A. Halim and G. Song, *Cancer Lett.*, 2017, **401**, 39–45.
228 L. Balaj, R. Lessard, L. Dai, Y.-J. Cho, S. L. Pomeroy, X. O. Breakefield and J. Skog, *Nat. Commun.*, 2011, **2**, 180.
229 B. K. Thakur, H. Zhang, A. Becker, I. Matei, Y. Huang, B. Costa-Silva, Y. Zheng, A. Hoshino, H. Brazier, J. Xiang,

C. Williams, R. Rodriguez-Barrueco, J. M. Silva, W. Zhang, S. Hearn, O. Elemento, N. Paknejad, K. Manova-Todorova, K. Welte, J. Bromberg, H. Peinado and D. Lyden, *Cell Res.*, 2014, **24**, 766–769.

230 I. Li and B. Y. Nabet, *Mol. Cancer*, 2019, **18**, 32.

231 W. Sun, Y. Ren, Z. Lu and X. Zhao, *Mol. Cancer*, 2020, **19**, 135.

232 M. Boyiadzis and T. L. Whiteside, *Leukemia*, 2017, **31**, 1259–1268.

233 A. Yokoi, A. Villar-Prados, P. A. Oliphint, J. Zhang, X. Song, P. De Hoff, R. Morey, J. Liu, J. Roszik, K. Clise-Dwyer, J. K. Burks, T. J. O'Halloran, L. C. Laurent and A. K. Sood, *Sci. Adv.*, 2019, **5**, eaax8849.

234 B. M. Chapin, P. Metola, S. L. Vankayala, H. L. Woodcock, T. J. Mooibroek, V. M. Lynch, J. D. Larkin and E. V. Anslyn, *J. Am. Chem. Soc.*, 2017, **139**, 5568–5578.

235 C. M. Renney, G. Fukuhara, Y. Inoue and A. P. Davis, *Chem. Commun.*, 2015, **51**, 9551–9554.

236 N. J. Hestand and F. C. Spano, *Chem. Rev.*, 2018, **118**, 7069–7163.

